HHS Public Access

Author manuscript

Dev Cell. Author manuscript; available in PMC 2020 January 28.

Published in final edited form as:

Dev Cell. 2019 January 28; 48(2): 229–244.e4. doi:10.1016/j.devcel.2018.12.015.

Axon-Dependent Patterning and Maintenance of Somatosensory Dendritic Arbors

Nelson J. Ramirez-Suarez[1], **Helen M. Belalcazar**[1], **Christopher J. Salazar**[1], **Burcu Beyaz**[2], **Benjamin Raja**[2], **Ken C.Q. Nguyen**[2], **Kevin Celestrin**[1], **Julius Fredens**[3], **Nils J. Færgeman**[3], **David H. Hall**[2], and **Hannes E. Bülow**[1,2,4,*]

[1]Department of Genetics, Albert Einstein College of Medicine, Bronx, NY 10461, USA

[2]Dominick P. Purpura Department of Neuroscience, Albert Einstein College of Medicine, Bronx, NY 10461, USA

[3]Department of Biochemistry and Molecular Biology, Villum Center for Bioanalytical Sciences, University of Southern Denmark, Odense M, DK-5230, Denmark

[4]Lead Contact

SUMMARY

The mechanisms that pattern and maintain dendritic arbors are key to understanding the principles that govern nervous system assembly. The activity of pre-synaptic axons has long been known to shape dendrites, but activity-independent functions of axons in this process have remained elusive. Here, we show that in *Caenorhabditis elegans,* the axons of the ALA neuron control guidance and extension of the 1° dendrites of PVD somatosensory neurons independently of ALA activity. PVD 1° dendrites mimic ALA axon guidance defects in loss-of-function mutants for the extracellular matrix molecule MIG-6/Papilin or the UNC-6/Netrin pathway, suggesting that axon-dendrite adhesion is important for dendrite formation. We found that the SAX-7/L1CAM cell adhesion molecule engages in distinct molecular mechanisms to mediate extensions of PVD 1° dendrites and maintain the ALA-PVDaxon-dendritic fascicle, respectively. Thus, axons can serve as critical scaffolds to pattern and maintain dendrites through contact-dependent but activity-independent mechanisms.

Graphical Abstract

*Correspondence: hannes.buelow@einstein.yu.edu.

AUTHOR CONTRIBUTIONS

N.J.R.S. and H.E.B. conceived the project. N.J.R.S. performed most experiments, except for electron microscopic studies (B.B., B.R., K.N., K.C., and D.H.H.) and proteomic studies (J.F. and N.J.F.). H.M.B. and C.J.S. contributed genetic data. N.R.J.S. and H.E.B. wrote the manuscript with editorial input from all authors.

SUPPLEMENTAL INFORMATION

Supplemental Information includes six figures, four tables, one video, and one data file and can be found with this article online at https://doi.org/10.1016/j.devcel.2018.12.015.

DECLARATION OF INTERESTS

The authors declare no competing interests.

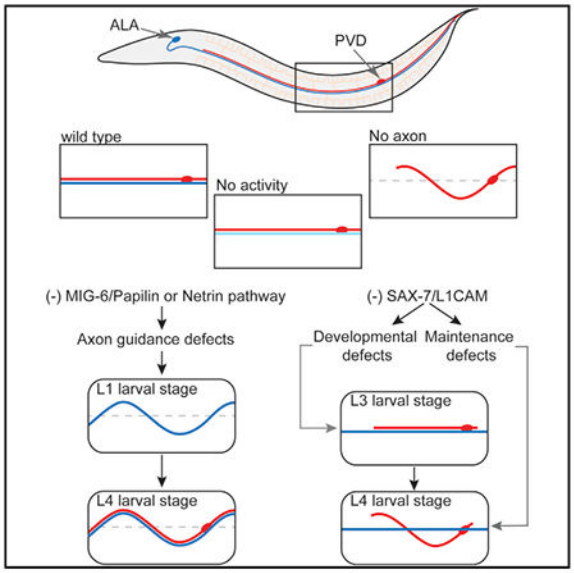

In Brief

The activity of presynaptic axons can shape dendrites, but whether axons also have activity-independent effects on dendritic patterning has not been clear. Ramirez-Suarez et al. now show that the axon of the ALA neuron in C. *elegans* patterns the dendrite of the PVD neuron through MIG-6/Papilin, Netrin, and SAX-7/L1CAM-mediated adhesion.

INTRODUCTION

Dendritic arbors are neuronal compartments that receive input from other neurons or the environment. Dendritic trees of individual neurons have distinct morphologies and their diverse shapes provide a key basis for neuronal identification and function.

Genetic approaches have uncovered both intrinsic and extrinsic factors that regulate patterning of dendritic arbors (Dong et al., 2015; Lefebvre et al., 2015). In addition, the neuronal activity of presynaptic partners has profound effects on dendritic arbors. For example, dendritic arborization of retinotectal neurons in *Xenopus* is inhibited when antagonists of N-methyl-D-aspartic acid glutamate receptors are administered during normal development (Rajan and Cline, 1998). Conversely, arborization increases in response to visual stimulation (Sin et al., 2002). Elimination of afferent axons or removal of neurotransmitter receptors that sense their signals disrupt the dendritic patterns in post-synaptic cells. In a classic example, spiny stellate neurons in layer IV of the rodent barrel cortex remodel their dendritic arbor after removal of either thalamocortical axons (Greenough and Chang, 1988) or post-synaptic NMDA receptors (Iwasato et al., 2000). Moreover, activity-regulated genes have the ability to induce structural changes in individual neurons, where they can act as positive (Zhou et al., 2006) or negative regulators of dendritic morphology (Ghiretti and Paradis, 2014). Whether axons can pattern dendrites independently of neuronal activity remains unknown.

The PVD somatosensory neurons in *C. elegans* are a pair of bilateral multidendritic neurons that sense harsh touch and extreme temperatures (Chatzigeorgiou et al., 2010; Mohammadi et al., 2013). PVD neurons are born post-embryonically during the early L2 larval stage in a lateral posterior position and, progressively develop elaborate dendritic arbors, initially through the formation of a 1° dendritic branch, which runs along the anterior-posterior axis in the lateral nerve tract. Subsequently, 2°, 3°, and 4° processes (also called high-order branches) emanate from the 1° branch in a series of orthogonal branching events to establish the stereotypic menorah-like arbors (Oren-Suissa et al., 2010; Smith et al., 2010; Albeg et al., 2011) (Figure 1A).

Genetic approaches have identified the Menorin pathway, which is important for PVD patterning. A complex of the SAX-7/L1CAM and the MNR-1/Menorin adhesion molecules acts instructively from the skin with the muscle-derived LECT-2/Chondromodulin-2 cytokine through the DMA-1/LRR-TM leucine rich transmembrane receptor in PVD neurons to pattern high-order dendritic branches of PVD (Dong et al., 2013; Salzberg et al., 2013; Díaz-Balzac et al., 2016; Zou et al., 2016). Using PVD as a model, we provide evidence of an activity-independent axonal mechanism, which, through basement membrane proteins and specific adhesion cues, control development and maintenance of a key determinant of dendritic arbor morphology, the 1° dendrite.

RESULTS

PVD 1° Dendrites Preferentially Associate with ALA Axons in the Lateral Nerve Tract

During embryonic development, a single ALA neuron in the head sends out one anteriorly directed process, which turns ventrally and bifurcates to send two posteriorly directed axons, one on each side of the body along the lateral mid-line (Wu et al., 2011). Meanwhile, the CANs, a bilateral pair of embryonically born cells, migrate to the mid-body region. There, they send two processes, one anteriorly and one posteriorly (Wu et al., 2011). During the post-embryonic L2 larval stage, the PVD 1° dendrite is added to the lateral nerve tract (White et al., 1986). Thus, in adult animals, the processes of the ALA neuron, CAN cells, and PVD comprise the lateral nerve tract (Figure 1A) (White et al., 1986).

Previous reconstructions of the *C. elegans* nervous system did not include detailed electron microscopic reconstructions of the lateral nerve cord (White et al., 1986). Thus, we analyzed the anatomical arrangement of the three neuronal processes in the lateral nerve cord, including possible connectivity, using serial section electron microscopy of wild-type animals (see STAR Methods). The geometry of the processes relative to their neighbors was variable along the anterior-posterior axis but tended to fall into two general patterns. The three neuronal processes were either stacked along a dorsal/ventral axis (Figure 1B) or in a tight group of three (Figure 1C). Less often, the lateral nerve tract was completely detached from the excretory canal (not shown). CANs tend to be closest to the excretory canal, while PVD was positioned more ventrally and ALA more dorsally, both usually adjacent to the pseudocoelom (Figures 1B–1G). ALA axons were distinguished by many periodic swellings along their length within the lateral nerves. Those swellings contained clusters of dense core vesicles (Figure 1C) and, rarely, a presynaptic density (Table S1), which is characteristic of active zones at most chemical synapses in *C. elegans.* It is more likely that their vesicular

release is non-synaptic and not directed toward specific post-synaptic targets. Rather, their peptidergic or neurotransmitter release likely enters both the pseudocoelom and affects multiple targets at a distance, although they may also locally affect CAN and/or PVD neurites in places where the epidermis wraps around and maintains the three neuronal processes isolated from other structures. Electrical synapses (gap junctions) were common along the CAN processes, especially to the epidermis, the excretory canal, and, to a lesser extent, to the ALA and PVD neuronal processes (Figures 1D–1G; Table S1). From the possible neuronal pairs, ALA-CAN formed the highest number of electrical synapses in the region surveyed (Figures 1D and 1E; Table S1), followed by ALA-PVD, which outnumbered CAN-PVD with regard to the number of electrical synapses (Figure 1F; Table S1).

Using fluorescent markers, we found that PVD 1° dendrites were significantly more often associated with ALA axons than with CAN processes (Figures 1H and 1I). However, we found no preferential association of ALA axons with either CAN processes or PVD 1° dendrites or CAN processes with ALA axons or PVD 1° dendrites (Figures 1H and 1I). These observations indicate specific associations and preferential connections for the processes in the lateral nerve tract: CAN processes more often associate with the excretory canal, whereas PVD 1° dendrites tend to associate more with ALA axons.

The ALA Neuron Is Required for Patterning of PVD 1° Dendrites

To examine whether ALA or CAN neurons are essential for PVD 1° dendrite development, we used laser ablation microsurgery at the L1 larval stage prior to the birth of PVD neurons. Early ablation of ALA cells resulted in 84% (n = 13) of ALA-ablated animals displaying PVD guidance defects with 1° dendrites meandering between the lateral nerve tract and the sublateral line that marks the boundary between muscle and epidermal cells (Figures 2A–2C). In addition, we found that 69% (n = 13) of 1° dendrites failed to fully extend in ALA-ablated animals (Figures 2A, 2B, and 2D). No comparable defects were seen in mock or CAN-ablated animals (Figures 2C and 2D).

To further corroborate this finding, we genetically ablated ALA neurons using a null mutation in the *ceh-17* gene, which encodes a Q50 paired-like homeobox transcription factor required for terminal differentiation of ALA neurons (Pujol et al., 2000). We found that *ceh-17* null mutant animals showed a PVD phenotype that was similar to ALA-ablated animals with 70% (n = 20) of PVD 1° dendrites displaying guidance defects and 100% (n = 20) extension defects, compared to 0% (n = 102) guidance defects and 0% (n = 33) extension defects in wild-type animals (Figures 2E and 2F; Table S2). The PVD phenotypes in *ceh-17* mutant animals could be transgenically rescued with a genomic copy of *ceh-17* (Figure S1). We conclude that *ceh-17* contributes to PVD 1° dendrite patterning through its role as a terminal selector for the ALA neuron, based on the following observations. First, previous work using antibody staining against CEH-17 and reporter experiments showed that CEH-17 is only expressed in ALA and SIA interneurons (Pujol et al., 2000). Second, transcriptomic profiling experiments found no *ceh-17* expression in PVD (Smith et al., 2010). Third, PVD cell fate markers *(dzIs53, F49H12.4p::mCherry* as well as its GFP counter-part *wdIs52)* are expressed normally in PVD (Figures 3C–3E). Conversely, CAN

processes were not affected in *ceh-17(np1)* mutants (Figures 2E and 2G) and disruption of CAN processes by a mutation in the *unc-39/Six4/5* family homeobox transcription factor (Yanowitz et al., 2004) failed to cause defects in PVD comparable to those in ALA-ablated animals (Table S2). We conclude that ALA axons are critical for PVD 1° dendrite patterning.

ALA Axons Pattern PVD 1° Dendrites in a Contact-Dependent Mechanism, Independently of Neuronal Activity

Differences between *ceh-17* mutant animals and ALA-ablated animals in PVD 1° branch development suggest that the previously reported variability in ALA axon outgrowth in *ceh-17* mutants (Pujol et al., 2000) might be their underlying cause. To determine whether contact with ALA axons contributes to patterning of PVD 1° dendrites, we compared the extension of the anterior PVD 1° dendrite in three different groups: *ceh-17(np1)* mutants where the underdeveloped ALA axon does not overlap with the PVD 1° dendrite, *ceh-17(np1)* mutants where the immature ALA axon overlaps with the PVD 1° dendrite, and wild-type animals with normally overlapping and fully mature ALA and PVD neurons. Animals without overlap between the ALA and PVD neurites produced shorter and misguided PVD 1° dendrites compared to animals with partial or full overlap (Figures 3A–3E). The less severe phenotype in animals with a partial overlap between ALA and PVD in *ceh-17* mutants suggests (1) that PVD 1° dendrite patterning is contact-dependent and (2) that factors independent of *ceh-17* serve additional functions during PVD 1° dendrite patterning.

We then asked whether ALA neuronal activity, neuropeptide release, or electrical coupling were required for PVD patterning. First, we analyzed null mutants for *vav-1*, a gene encoding a guanine nucleotide exchange factor for Rho-family GTPases that is required for both the excitation and the activation of the ALA neuron (Fry et al., 2014). Second, we analyzed transgenic animals expressing a tetanus toxin light chain in ALA, which blocks the release of all vesicles containing neurotransmitters and neuropeptides (Schiavo et al., 1992). Third, we examined loss-of-function mutants of genes encoding proteins involved in the processing or secretion of neuropeptides such as the proprotein convertase EGL-3, the carboxypeptidase EGL-21, the peptidyl glycine alpha-amidating monooxygenase PAMN-1, and the UNC-31/CAPS calcium-dependent activator protein. Fourth, ALA neurons are GABAergic (Gendrel et al., 2016), PVD neurons express GABA receptors (Smith et al., 2010), and GABA has been suggested to serve extrasynaptic developmental functions by way of GABA receptors (Owens and Kriegstein, 2002). We thus interrogated mutants in *unc-25,* the gene encoding the sole gamma aminobutyric acid (GABA) biosynthetic enzyme glutamic acid decarboxylase, for defects in PVD. Fifth, we examined loss-of-function mutants for *unc-7* and *unc-9,* which encode two innexins and show widespread expression in the nervous system including ALA, PVD, and CAN neurons (Altun et al., 2009; Bhattacharya et al., 2019) as well as mutants for a dominant negative allele for the somatostatin-like protein gene *unc-1,* known to silence UNC-9-mediated gap junctions (Jang et al., 2017). None of these manipulations caused abnormalities in PVD comparable to those seen in ALA-ablated animals (Figures 3F–3I). These findings suggest that ALA neuronal activity is dispensable for PVD 1° dendrite patterning, although we cannot exclude

redundancy or the possibility of additional ALA- or PVD-expressed innexins playing a role in PVD 1° branch development or maintenance.

PVD 1° Dendrites Are Patterned by MIG-6/Papilin Together with the Netrin Pathway

To identify factors that are important for PVD 1° dendrite patterning, we conducted a proteomic screen (Figure S2) and identified MIG-6/Papilin, a conserved extracellular matrix protein required for distal tip cell migration (Kawano et al., 2009) and pharynx organogenesis (Jafari et al., 2010). The *mig-6* locus encodes a long and a short isoform (Figure 4A) (Kawano et al., 2009). The *mig-6(ev788)* deletion allele is homozygous lethal, but heterozygous animals display severe defects in PVD 1° dendrite guidance with processes that deviate from their normal trajectories and meander between the ventral and dorsal 3° PVD dendritic branches (Figures 4B and 4D). Similar results were obtained upon post-embryonic knock down of *mig-6* in wild-type animals by RNA interference (RNAi) (Figure S2). Removing the long isoform alone using two different non-sense mutant alleles *(e1931* and *oz113)* did not produce comparable phenotypes in PVD either in a dominant or recessive manner (Figure 4D). These findings show that (1) the *mig-6* locus is haploinsufficient and a minimum level of MIG-6/Papilin is required for proper PVD 1° guidance, (2) the zygote-derived long isoform is not required for PVD patterning, and (3) MIG-6/Papilin function is required post-embryonically. Two missense alleles *(ev700* and *ev701)* changing conserved cysteine residues in the lagrin repeats produced a fully dominant phenotype compared to heterozygotes of the putative null allele *ev788* where the penetrance is around 50% (Figure 4E; Table S2). This indicates that the *ev700* and *ev701* alleles are dominant negative in this cellular context, as in gonad patterning (Kawano et al., 2009). Interestingly, we did not observe comparable defects in two different alleles of *mig-17/ADAM* (Figure S2), a metalloproteinase that is localized by MIG-6/Papilin during gonad development (Kawano et al., 2009). Thus, MIG-6/Papilin employs distinct mechanisms to control PVD 1° dendritic and gonad development.

A second set of mutants known to display similar defects in PVD 1° dendrites are in genes of the Netrin pathway. The UNC-6/Netrin ligand and its UNC-40/DCC and UNC-5/Unc5 receptors are required for the correct positioning of PVD 1° dendrites (Smith et al., 2012). We confirmed these results and found that the phenotype in *unc-40; unc-5* double mutants was not further enhanced compared to the single Netrin receptor mutants (Figures 4C and 4F). Moreover, trans-heterozygous animals for *mig-6* and *unc-6* null alleles showed an enhanced PVD 1° guidance phenotype compared to individual heterozygous mutant animals (Figure 4G). Collectively, these findings suggest that *mig-6/Papilin* and Netrin signaling act genetically in the same pathway to pattern PVD 1° dendrites.

MIG-6/Papilin Is Expressed along the Lateral Nerve Tract

A rescuing fluorescent mNeonGreen::MIG-6S fusion (Figure S3) is localized to longitudinal nerve tracts such as the lateral nerve and the sublateral tracts (Figures 4H–4J). The precise colocalization of mNeonGreen::MIG-6S with the PVD 1° dendrite suggests that the extracellular matrix and perhaps the basement membrane adjacent to these neuronal tracts may be where MIG-6/Papilin functions to pattern PVD 1° dendrites. Transgenic expression of MIG-6S under control of its own promoter *(mig-6p$_{(5.4kb)}$)* or a pan-neuronal (*rab-3p*)

promoter rescued PVD defects but not its expression in either CAN *(ceh-23p$_L$)*, ALA *(ida-1p),* or PVD neurons *(ser-2p$_{3s}$)*, or in body wall muscle *(myo-3p)* (Figure S3). These experiments suggest that for correct patterning of PVD 1° dendrites, MIG-6/Papilin needs to be expressed in a combination of neurons or at levels only achieved when expressed by multiple cells.

ALA Axons Are Patterned by MIG-6/Papilin Together with the Netrin Pathway

We next asked whether the defects in PVD 1° dendrites were a reflection of defects in ALA patterning. We found that *mig-6/Papilin* and Netrin mutants displayed defects in the positioning of ALA axons that predicted the effects on the positioning of PVD 1° dendrites (Figures 5A–5D). The ALA neuron is born early in embryo-genesis and completes its development 12 h before PVD is born (Smith et al., 2010; Albeg et al., 2011; Wu et al., 2011). Given that PVD 1° dendrite extension and localization depend on ALA, we proposed that the PVD defects seen in the *mig-6/Papilin* and Netrin pathway mutants were secondary to defects in ALA axon patterning. In support, we found that *mig-6/Papilin* and Netrin mutants presented ALA axon positioning defects at early larval stages, before PVD was born (Figures 5E and 5F), suggesting that the defects present in ALA axons are “copied” by the PVD 1° dendrite throughout the dendrite guidance process. CAN cells were also affected but by and large maintained their association with the PVD 1° dendrite in these mutants (Table S2), indicating that the observed phenotypes can be generalized to the lateral nerve tract. To investigate where Netrin pathway factors may function to pattern ALA axons, we analyzed *unc-6* and *unc-40* fosmid-based transcriptional reporter transgenes (Weinberg et al., 2018). We found that at the early L1 larval stage, the *unc-6* reporter is expressed in several cells in the head but not in ALA neurons (Figure 5G), whereas the *unc-40* reporter was clearly expressed in ALA neurons (Figure 5H). Moreover, we observed transgenic rescue of ALA axon defects in *unc-6* mutants using a genomic copy of *unc-6* (Figure 5I) and, in *unc-40* mutant animals expressing the *unc-40* cDNA specifically in ALA (Figure 5J). Taken together, our anatomical, ablation, genetic, and transgenic rescue experiments show that (1) the ALA axons provide a substrate for PVD neurons to guide and extend their 1° dendrites, (2) *mig-6/Papilin* and the *unc-6/Netrin* pathway act together to guide the ALA axons, and (3) the *unc-40/DCC* netrin receptor functions cell-autonomously in ALA, whereas the *unc-6/Netrin* ligand functions non-autonomously.

SAX-7/L1CAM Functions in ALA to Promote PVD 1° Dendrite Extension

The intimate association between the ALA axon and the PVD 1° dendrite implies that dedicated mechanisms must exist that allow the PVD 1° dendrite to identify its substrate, initiate branching, extend the process along the axon, and maintain fasciculation between both processes. To identify factors involved in these mechanisms, we interrogated several mutant alleles of genes known to be required for patterning of higher-order branches in PVD neurons (Dong et al., 2013; Salzberg et al., 2013). Among the candidates, we identified the immunoglobulin (Ig) domain cell adhesion molecule SAX-7/L1CAM (Figure 6A) as a key factor for extension and association of the PVD 1° dendrite with ALA axons. We next asked whether the long or short SAX-7 isoforms were essential for dendrite extension during PVD 1° formation. To this end, we used the *sax-7(nj48)* and the *sax-7(dz156)* alleles, which affect both isoforms, while the deletion *sax-7(nj53)* allele was used to interrogate the significance

of the long isoform (Figures 6C and 6D). In analogy to the findings for patterning of higher-order branching, we found that loss of both the SAX-7L long and SAX-7S short isoforms, but not the SAX-7L long isoform alone or the paralogous Ig domain containing single-transmembrane protein LAD-2, resulted in defects in PVD 1° dendrite extension, where the posterior and, less often, the anterior 1° dendrites were significantly shorter (Figures 6B–6D and S4; Table S2).

From the early L3 larval stage onward, when the PVD 1° dendrite has just reached its full extension in wild-type animals (Smith et al., 2010), none of the posterior 1° dendrites are fully extended in *sax-7/L1CAM* mutant animals (length of posterior 1° dendrite ≤ 100 μm in 100% of PVDs in *sax-7(nj48)* versus 0% in control animals, n = 50 (Figure 6E)). Because we observed no dendrite retraction in time-lapse analyses of L3 *sax-7* mutant larvae (Video S1), we conclude that the *sax-7/L1CAM* phenotypes result from PVD 1° dendrite extension defects rather than excessive pruning.

To further analyze the genetic mechanisms of dendrite extension, we focused our analyses on the posterior 1° dendrite. We found similar defects in mutants of the Menorin pathway such as *mnr-1/Menorin, dma-1/LRR-TM,* or *lect-2/Chondromodulin II* (Figures S4A and S4B; Table S2). Similarly, recently described downstream effectors for the Menorin pathway involved in high-order branching patterning (Zou et al., 2018; Tang et al., 2018) also play a role in PVD 1° extension. For example, null mutants for *tiam-1*, the *C. elegans* homolog of the multidomain vertebrate Rac1 guanine nucleotide exchange factor (GEF) Tiam1 and for the Claudin homolog *hpo-30,* presented highly penetrant extension defects comparable to the phenotype observed for *sax-7/L1CAM, mnr-1/Menorin,* and *dma-1/LRR-TM* single mutants (Figures S4A and S4B). A missense allele of *act-4/Actin (dz222,* G151E), identical to the *act-4(wy917)* allele reported to produce abnormalities in high-order branch patterning (Zou et al., 2018), did not cause extension defects in mutant animals. However, it has been reported that induced actin depolymerization *in vivo* affected PVD 1° extension of both anterior and posterior branches (Harterink et al., 2017), implying that actin does have a role in 1° dendrite outgrowth.

To better understand the genetic interactions of *sax-7/L1CAM* with other members of the Menorin pathway in the context of PVD 1° branch development, we quantified the complete absence of the posterior 1° branch in single and double mutants as a readout for branch initiation and extension defects. Mutants in *dma-1/LRR-TM,* but not *sax-7/L1CAM* or *mnr-1/Menorin* singles, showed a moderate number of affected PVDs (30% n = 57 for *dma-1* mutants versus 0% n = 30 for controls, Figures S4C and S4D). Similar to observations for high-order branches, double null mutants of *dma-1* with *sax-7* or *mnr-1* did not enhance the defects observed in *dma-1* singles, and double mutants of *sax-7/L1CAM* with *mnr-1/Menorin* did not present synthetic phenotypes (Figure S4C). Furthermore, loss of *hpo-30/Claudin* in a *dma-1/LRR-TM* null background failed to enhance the observed 1° initiation/extension defects or generate the synthetic defects seen when combined with *sax-7/L1CAM* null alleles, suggesting that *hpo-30* acts as part of the Menorin pathway to promote branch extension. Interestingly, double mutants between *sax-7/L1CAM* or *mnr-1/Menorin,* and *tiam-1* or *act-4* alleles generated a dramatic synthetic phenotype where a significant increase of PVDs lacking posterior 1° dendrites was observed (Figure S4D), a

scenario that was also present in *dma-1; act-4* double mutants. Altogether, these results suggest that (1) SAX-7/L1CAM functions through the canonical Menorin pathway during PVD 1° dendrite extension and (2) *act-4* and *tiam-1* may serve in a parallel pathway to *sax-7/L1CAM* during initiation/extension of the PVD 1° dendrite.

Next, we asked where SAX-7/L1CAM functions to promote PVD 1° dendrite extension. We found that, consistent with enrichment of *sax-7/L1CAM* transcripts in PVD (Smith et al., 2010) and ALA (Nath et al., 2016), a SAX-7::GFP translational reporter was expressed in both the ALA and PVD processes (Figures 7A and 7B). Transgenic expression of SAX-7S in ALA or all neurons, but not in PVD, the epidermis (skin), or CAN, rescued extension defects in PVD 1° dendrites but not high-order branches (Figures 7C, 7E, and S4E). In contrast, expression in the epidermis (skin) rescued the formation of high-order PVD dendrites as previously reported (Dong et al., 2013; Salzberg et al., 2013), but failed to rescue PVD dendrite extension along the ALA axon (Figures 7C, 7F, and S4E). Instead, expression of SAX-7S in the epidermis resulted in PVD 1° dendrites that extended but deviated from their regular trajectory and grew along the edge of the lateral epidermal ridge (Figure 7F), where SAX-7 is locally enriched (Dong et al., 2013; Salzberg et al., 2013). This phenotype is also observed in ALA-ablated animals (Figure 2B) and in *ceh-17* mutants (Figures 2E, 3D, and 3E), possibly because the only source of high levels of SAX-7/L1CAM in these animals is at the edge of the epidermal ridge, rather than in ALA. We suggest that SAX-7S functions non-autonomously to mediate PVD 1° dendrite extension. Two additional lines of evidence suggest that SAX-7/L1CAM functions through a similar mechanism in PVD 1° extension and patterning of high-order branches. First, both processes required Fibro-nectin III (FNIII) domains but neither the Ig domains nor the intracellular domain of SAX-7/L1CAM (Figure 7D). Second, the binding partner for SAX-7/L1CAM, MNR-1/Menorin, is expressed in ALA (Figure S4F) in a *cis* configuration shown to be required for an instructive signal through the DMA-1/LRR-TM receptor (Salzberg et al., 2013). We conclude that SAX-7/L1CAM functions in ALA axons and acts mechanistically through the Menorin pathway to mediate extension of PVD 1° dendrites. Of note, even in the absence of Menorin pathway activity, the PVD anterior 1° branch is still able to extend. Therefore, additional mechanisms must exist that control 1° dendrite outgrowth, consistent with a previous report showing that the *clr-1*/Receptor Tyrosine Phosphatase functions in parallel to the Menorin pathway for PVD 1° outgrowth (Liu et al., 2016).

SAX-7/L1CAM Functions in ALA Axons and PVD 1° Dendrites to Maintain Fasciculation

Interestingly, *sax-7/L1CAM* null mutants also showed severe fasciculation defects between PVD 1° dendrites and ALA axons, which retained their original localization in the lateral nerve tract (Figures 6A–6C). Again, ALA-PVD fasciculation did not require the SAX-7L long isoform alone or the paralogous LAD-2 cell adhesion molecule (Figures 6C and 6F; Table S2), and no comparable defects were seen in mutants for genes of the Menorin pathway such as *mnr-1/Menorin, dma-1/LRR-TM, lect-2/Chondromodulin II* (Figure S5A; Table S2), or *mig-6/Papilin* and *unc-6/Netrin* (Table S2). These findings indicate that the short isoform of SAX-7S is required for fasciculation of the PVD 1° dendrites with ALA axons, whereas the Menorin pathway, MIG-6/Papilin, or Netrin play no major role in this process individually.

SAX-7/L1CAM could function during development or maintenance of the PVD/ALA fascicle. We found that the percentage of fasciculation defects between ALA axons and PVD 1° dendrites in *sax-7/L1CAM* mutant animals dramatically increased from the early L3 larval to the late L4 larval stage (30.4% defects [n = 23] at L3 versus 95.8% [n = 24] at L4), whereas neither early fasciculation defects nor an increase in PVD-ALA association from the L3 to L4 larva stage was observed in wild-type control animals (4.3% [n = 23] at L3 versus 0% [n = 23] at L4) (Figure 6G)). These observations suggest that SAX-7S/L1CAM maintains fasciculation between the PVD 1° dendrite and ALA axons, although additional functions of SAX-7/L1CAM in this context during development are possible.

The ALA-PVD fasciculation defects in *sax-7/L1CAM* mutants were fully rescued by pan-neuronal expression of *sax-7/L1CAM* but not by epidermal expression (Figures 7E and S5B). Expression of SAX-7S in ALA, but not in PVD, partially rescued neurite fasciculation defects. However, a robust rescue was observed when SAX-7S was expressed in both ALA and PVD neurons (Figures 7E and 7G). Rescue with SAX-7S appeared dosage sensitive: reducing the DNA concentration in rescuing transgenes by half, we found that individual expression of SAX-7S in ALA, PVD, or CAN had little effect, although panneuronal expression of SAX-7S still rescued both PVD 1° dendrite extension and ALA-PVD fasciculation defects (Figure S5B). Again, the functions of SAX-7/L1CAM to maintain fasciculation required the FNIII domains, but not the Ig domains or the intracellular domain (Figure 7H). Thus, *sax-7/L1CAM* maintains the ALA-PVD fascicle by functioning either in ALA or, in ALA and PVD independently of its intracellular signaling domain.

DISCUSSION

We show here that the axon of the ALA neuron patterns the PVD 1° dendrite in a process that is independent of either neuronal activity or neuropeptide release. The ALA axons themselves are guided by the conserved extracellular matrix protein MIG-6/Papilin in conjunction with the Netrin system of axon guidance ligands and receptors. Intriguingly, the neural cell adhesion molecule SAX-7/L1CAM plays a dual role in patterning the PVD 1° dendrite, namely a developmental role during extension of the dendrite along the axon, and a post-developmental role in the maintenance of axon-dendrite fasciculation.

MIG-6/Papilin Functions with the Netrin Pathway to Pattern the Lateral Nerve Tract

ALA, CAN, and PVD neurites require MIG-6/Papilin and the Netrin pathway for proper patterning, likely to both establish and maintain the lateral nerve tract. First, defects in the PVD 1° dendrite are present in *mig-6/Papilin* mutants at early developmental stages, suggesting a developmental role for MIG-6/Papilin. Second, knockdown experiments during post-embryonic larval stages showed that sustained expression of *mig-6/Papilin* is required from the L1 stage onward to maintain the position of the lateral nerve tract. MIG-6/Papilin is a large conserved extracellular matrix protein with structural similarity to ADAMTS secreted matrix-associated metalloproteinases and has been implicated in organogenesis of *C. elegans* (Kawano et al., 2009; Jafari et al., 2010) and Drosophila (Kramerova et al., 2000). However, beyond a role for MIG-6/Papilin in localizing the ADAM metalloproteinase MIG-17 during gonad patterning in *C. elegans* (Kawano et al., 2009), the functions of

Papilins have remained elusive. Our finding that MIG-6/Papilin is important for forming and maintaining a specific nerve tract in conjunction with the UNC-6/Netrin signaling cassette of axon guidance factors adds to our understanding of this basement membrane protein. A plausible scenario for neuronally derived MIG-6/Papilin is that this molecule establishes a specialized local basement membrane that could, in turn, capture secreted UNC-6/Netrin to guide ALA and CAN processes. This scenario is consistent with reports suggesting that Netrin can be captured non-autonomously in flies to guide axons (Hiramoto et al., 2000) or that it can provide a substrate to guide commissural axons during mouse embryonic spinal cord development (Dominici et al., 2017; Varadarajan et al., 2017).

The Multiple Facets of SAX-7/L1CAM in Dendrite Patterning

The outgrowth of PVD 1° dendrites on ALA axons and maintenance of the ALA-PVD fascicle requires dedicated molecular mechanisms. We found that SAX-7/L1CAM promotes the outgrowth of the posterior 1° dendrite acting from the ALA axon in a mechanism that is also dependent on the Menorin pathway. SAX-7/L1CAM provides topological information that guides different types of dendritic branches in PVD. It functions in the epidermis to promote high-order branching (Dong et al., 2013; Salzberg et al., 2013; Liang et al., 2015) but also functions in ALA and PVD to promote PVD 1° patterning (Figure S6). It is thus possible that the fasciculation of a subgroup of PVD 2° branches with motor neuron commissures that seems to be independent of genes in the Menorin pathway (Smith et al., 2013) depends on a SAX-7-mediated mechanism as well.

SAX-7/L1CAM has previously been shown to maintain cell soma position and the integrity of the ventral nerve cord (Sasakura et al., 2005; Wang et al., 2005; Pocock et al., 2008). Surprisingly, maintaining ALA-PVD fasciculation required the FNIII domains but not intracellular domain or the Ig domains. This is in contrast to findings for SAX-7/L1CAM in maintaining cell soma position, which required the Ig domains and the intracellular domain but not the FNIII domains (Pocock et al., 2008; Díaz-Balzac et al., 2015). Thus, SAX-7/L1CAM functions through molecularly distinct mechanisms to maintain axo-dendritic fasciculation and cell soma position.

The most parsimonious explanation for the functions of SAX-7/L1CAM in maintaining ALA-PVD axo-dendritic fasciculation is through homophilic interactions. Alternatively, SAX-7/L1CAM may be only required in ALA, and the improved rescue by expression in ALA and PVD is a consequence of homophilic interactions due to overexpression of this cell adhesion molecule. Either explanation is consistent with a role of SAX-7/L1CAM in ALA, whether it interacts with other SAX-7/L1CAM molecules or with additional partners located in trans to maintain ALA-PVD fasciculation. Heterophilic interactions involving SAX-7 are not uncommon. In fact, RIG-6/Contactin (Kim and Emmons, 2017), KAL-1/Anosmin-1 (Díaz-Balzac et al., 2015), LECT-2/Chondromodulin II (Zou et al., 2016), and STN-2/γ-syntrophin (Zhou and Chen, 2011) bind SAX-7/L1CAM to mediate different aspects of nervous system development. Thus, SAX-3/Robo described in the companion paper (Chen et al., 2019) could be a factor mediating ALA-PVD association through *trans* interactions with SAX-7/L1CAM in ALA axons. Alternatively, human L1CAM has been shown to trimerize via its FNIII domain to then interact with heteromeric integrin complexes

(Silletti et al., 2000), thus providing putative candidates for additional heterophilic partners of SAX-7/L1CAM function in ALA-PVD axo-dendritic fasciculation. Regardless, the functional significance of FNIII domains in this type of cell adhesion molecules may be conserved since mutant mice lacking the Ig domains in L1CAM (and therefore their canonical Ig-domain-mediated homophilic interactions) do not present many of the neuronal defects that characterize animals lacking all L1CAM function (Itoh et al., 2004).

Axons Pattern Dendrites Independent of Activity

Neuronal activity is a major post-embryonic driving force involved in the development and plasticity of synaptic connections (Sin et al., 2002; Wong and Ghosh, 2002). In contrast, activity-independent molecular interactions are primarily responsible to shape earlier aspects of nervous system development (Wong and Ghosh, 2002). At earlier stages, neuronal processes are highly responsive to cues from neighboring cells (Schmidt et al., 2014; Constance et al., 2018). For example, neurons in the visual nervous system of mice follow adhesive cues provided by their presynaptic partners (Peng et al., 2017). In cases where the target tissue is at a distance, adhesion to guidepost cells facilitates the proper formation and maintenance of extending neurites. Axons, for instance, are guided, sorted, or shaped by interactions with other axons (Hayashi et al., 2014; Siegenthaler et al., 2015). In contrast, scarce evidence exists for a role of axons in patterning dendritic structures, although genetic observations and early irradiation experiments suggested that granule neurons are required for a correct patterning of the Purkinje dendritic tree (Altman and Anderson, 1972).

Axons can communicate with dendrites in different ways. Besides chemical and electrical synapses (gap junctions), non-synaptic chemical neurotransmission through neuropeptides can happen along the axonal processes (Arce et al., 1992; Uhlrich et al., 1993). Our observations indicate that the ALA neuron may use all three of these modalities to communicate with its neighbors. The non-synaptic release of dense core vesicle from axonal swellings seems to represent the main, but not the exclusive form, of ALA axonal activity. Regardless of whether and how ALA and PVD communicate, our findings show that axons can serve as critical scaffolds to pattern and maintain dendrites in an activity-independent manner. It has recently been found that positioning of the initial dendritic branching point of the aCC motoneurons in Drosophila is defined by the intersection of the aCC motorneuron dendrite with an axon (Kamiyama et al., 2015). Thus, contact-dependent, yet activity-independent interactions between the myriad of axons and dendrites that form the nervous system could represent a more general and conserved principle where preassembled axonal tracts direct aspects of both development and maintenance of newly forming dendritic processes.

STAR★METHODS

CONTACT FOR REAGENT AND RESOURCE SHARING

Further information and requests for resources and reagents should be directed to and will be fulfilled by the Lead Contact, Hannes E. Bülow (hannes.buelow@einstein.yu.edu).

EXPERIMENTAL MODEL AND SUBJECT DETAILS

***C. elegans* Handling—**N2 Bristol was used as the wild type strain, animals were raised at 20 °C under standard conditions on NGM plates using *Escherichia coli* strain OP50. Phenotypic analysis was performed in L4 hermaphrodites (unless noted otherwise). For details and a complete list of strains used and generated in this study, see Table S3.

METHOD DETAILS

Molecular Biology and Transgenesis—For details on Molecular Biology Methods or reagents used and generated in this study, see Key Resources Table and Table S4.

Transgenic ceh-17 Rescue of PVD 1° Dendrite Defects—A PCR product covering the entire *ceh-17* genomic locus including 2235bp upstream of its transcription start site and 783bp downstream its putative stop codon (for primer information see Table S4) was injected at 5 ng/µl into *ceh-17(np1) I; dzIs53 II; inIs181; inIs182 IV,* together with the *myo-3p*::GFP marker at 25 ng/µl and *pBluescript* at 70 ng/µl.

Heterologous Rescue of mig-6 PVD 1° Dendrite Defects—The *mig-6s genomic/cDNA* from *pZH125* (kind gift of Joe Culotti)(Kawano et al., 2009) was cloned under control of heterologous promoters: ALA-specific *ida-1p* (Pujol et al., 2000), PVD-specific *ser-2p*$_{3s}$ promoter (Tsalik et al., 2003), CAN-specific *ceh-23p*$_{L}$ (Wenick and Hobert, 2004) and pan-neuronal *rab-3p* (Nonet et al., 1997). All constructs were injected at 5 ng/µl into *dzIs53 II; mig-6(ev700) V,* together with the *myo-2p*::mCherry marker at 25 ng/µl and *pBluescript* at 70 ng/µl.

Translational Reporter of mig-6/Papilin—*pZH125* (kind gift of J. Culotti) was digested with *Eco47III/NcoI* and a Gibson assembly reaction was performed with the larger digested fragment plus three PCR products (A+B with *pZH125* as template, C+D with *pDD268* as template and E+F with *pZH125* as template, (see primers Table S4). The newly assembled plasmid differs from *pZH125* in that it includes a mNeonGreen fluorescent tag inserted in frame between serine 65 and valine 66 of the M\G-6/Papilin sequence. This construct was injected into EB1982 animals at 5 ng/µl and *pBluescript* at 95 ng/µl and the resulting extrachromosomal array was outcrossed using *dzIs53 II; inIs181 inIs182 IV; dpy-11(e224) mig-6(ev788) V /eT1 nIs267 III V* animals to generate *dzIs53; dpy-11(e224)mig-6(ev788) V; Ex [mig-6p::mNeonGreen::mig-6s]* homozygous mutants for the *mig-6* null allele.

Heterologous Rescue of unc-6/Netrin and unc-40/DCC Defects—The *unc-40* cDNA (kind gift of C. Bénard) was cloned under control of the ALA-specific *ida-1p* and was injected at 5 ng/µl into *unc-40(e271) I; dzIs53 II; inIs181 inIs182 IV* together with the *myo-2p::mCherry* marker at 25 ng/µ! and *pBluescript* at 70 ng/µl. A plasmid containing the *unc-6* genomic region (kind gift of W. Wadsworth) was injected at 5 ng/µl into *dzIs120 IV; unc-6(ev400) X* together with the *myo-2p::mNeonGreen* marker at 25 ng/µl and *pBluescript* at 70 ng/µl.

Heterologous Rescue of sax-7 PVD 1° Dendrite Defects—The *sax-7* cDNA was cloned under control of heterologous promoters: ALA-specific *ida-1p* (Pujol et al., 2000), PVD-specific *ser-2p3* (Tsalik et al., 2003), epidermal *dpy-7p* (Gilleard et al., 1997) and pan-neuronal *rab-3p* (Nonet et al., 1997). All constructs were injected at 5 ng/μl into *dzIs53II*; *sax-7(nj48) inIs181 inIs182 IV* together with the *myo-2p::mCherry* marker at 25 ng/μl and *pBluescript* at 70 ng/μl. For additional details on plasmids or fusion constructs see Key Resources Table.

Transmission Electron Microscopy—The lateral nerve was studied in serial thin sections by TEM using a Philips CM10 electron microscope and an Olympus Morada digital camera system. Young adult animals from several different fixation methods were compared, including 8 animals in total. N2 animals were fixed by standard chemical immersion methods (Hall, 1995), while *him-5* animals were fixed by high pressure freezing and freeze substitution (Hall et al., 2012). Thin sections were collected on slot grids, post-stained, and viewed by TEM. The *him-5* mutation appeared to have no effect on the appearance of the nerve and the intimate contacts between the neuronal processes and nearby tissues and is therefore considered wild type. Both methods provided high quality images of cell outlines, contents of the neuronal cytoplasm and their intercellular contacts. To improve chances to identify all neurons, sections were viewed from the midbody region in vicinity of the CAN soma (Figure 1), so that the CAN processes could be traced to the soma. ALA processes were easily recognized by their increased number of dense-core vesicles (Figure 1C), and PVD by occasional local 2° branches (Figures 1B and 1F). To avoid any confusion with the process of SDQL, all data were collected from the right side lateral nerve, which has no SDQ process in that midbody locale.

Cell Ablations—Two strains were generated for cell ablation experiments, the first one expressed a translational IDA-1::GFP fusion driven by the *ida-1* promoter allowing visualization of the ALA soma and its axonal processes with a distinctive punctate pattern described previously for this dense core vesicle resident protein (Zahn et al., 2004). The second strain carries a transcriptional reporter where GFP was expressed under the *kal-1* promoter sequence, known to drive expression in uterine cells, excretory cells, in several neurons as well as the CAN cells (Bülow et al., 2002).

Synchronized L1 animals expressing a cytoplasmic GFP fluorescent marker in ALA or CAN cells, and a mCherry cytoplasmic marker in PVD were immobilized using 1mM levamisole (Sigma). The ALA cell body or a single CAN cell body was targeted with a high-energy laser using a Pulsed UV, Air-Cooled, Nitrogen Laser System (Spectra-Physics). Three pulses separated by 5-second intervals were applied. Successful targeting events were verified by visual inspection of fluorescence quenching. For mock ablations, the laser was targeted to a more ventral position located a cell-body distance of the ALA soma using the same firing protocol. For CAN cell ablations, the contralateral side (non-ablated side) was used as experimental control. Animals were recovered from slides and allowed to grow for 47-57 hours until they reached the L4/young adult stage. Successful ablation was verified by absence of cell-specific fluorescence and followed by quantification of PVD 1° dendrite defects in extension and guidance.

Imaging—Fluorescent images of live *C. elegans* were captured using a Plan-Apochromat 40×/1.4 objective on a Zeiss Axioimager Z1 Apotome. Worms were immobilized using 1mM levamisole (Sigma) and *Z* stacks were collected. Maximum intensity projections of L1 or L4/young adult animals were used as indicated except for colocalization studies where single optical sections of two-days-old adult animals were used.

For quantification of neurite proximity, a triple labeled extrachromosomal strain (EB3312) was used. Z stacks of the lateral nerve tract in this experiment used 0.45μm steps and the same exposure time for each channel between animals. Animals were traced to identify the 100μm section anterior to the PVD cell body. Using the orthogonal view option in the ImageJ software, proximity was quantified every 5μm along the 100μm segment. A total of 20 different sections per neurite pair were interrogated for the presence or absence of adjacency/overlap between different pairs of neuronal processes. Proximity index for a given pair of neurites was calculated as the fraction of total sections (n = 20) quantified per animal in which proximity was visible for that specific pair of neurites. Statistical pairwise comparisons were computed between pairs formed by a specific neurite and each of the two possible companion processes to determine which of them was more likely to be in close proximity.

For time lapse imaging, *sax-7(nj48)* mutants at the early L3 stage (identified by gonadal development) were immobilized on 10% agarose pads with polystyrene beads (Polyscience, 2.6% by volume, 0.1 μm diameter) (Kim et al., 2013). Around cover glass (12mm diameter) was used and sealed with petroleum jelly to preserve preparation moisture during long-term imaging. A region including the PVD somata was imaged for three hours at 5 min intervals starting at the beginning of L3 when the 1° dendrite has just reach its total extension in normal conditions. Z-projections (0.5μm/step) spanning the focal depth of the neuron, were collected using a 63× objective. Movies were obtained using an inverted Nikon TE2000-S microscope equipped with a Perkin-Elmer UltraVIEW spinning disk unit. Volocity software (version 6.2.1) was used to collect the raw files and processing and video editing were carried out using the Image-J 1.46r software.

RNAi—Bacterial RNAi clones were grown overnight and seeded onto agar plates containing 1mM isopropyl β-D-1-thiogalactopyranoside (IPTG) (Sigma) and 50 mg/μl carbenicillin and allowed to dry for 24 to 48 hours at room temperature. For L1 RNAi, L1 synchronized hermaphrodites (50) were placed on RNAi-seeded plates and analyzed 47-57 hours later, after reaching L4/young adult stage.

SILAC—Stable isotope labeling with Amino acids was performed in three different strains: wild type (Lys0), *kpc-1* homozygous mutants *(dz182* allele, (Salzberg et al., 2014)) (Lys4) and rescued animals expressing *kpc-1* specifically in PVD (Lys8) following a protocol previously adapted for nematodes (Fredens et al., 2011). Detection of peptides by mass spectrometry and assignment of these peptides to specific proteins produced a list of 3604 proteins (Figure S2). This list was reduced to 1965 candidates that included proteins that had a 1% or less risk of being misidentified and that were found in at least two biological replicates. From this list, we selected proteins that showed different relative levels between the *kpc-1* mutant and wild type animals (188 candidates). Among those we selected the

protein candidates that showed different relative levels between *kpc-1* mutant and rescued animals (130 candidates). Finally, we examined the candidates and divided this group in two: 63 proteins with a similar relative amount of the candidate protein in rescued vs wild type animals and 67 proteins with a different relative amount of the candidate protein in rescued animals when compared to wild type animals (Figure S2). 109 out of 130 had available RNAi clones in commercial libraries and we used those clones to assess suppression of the *kpc-1* mutant phenotype in a hypomorphic mutant *(gk333538* allele) strain or phenocopy of the *kpc-1* mutant phenotype in a wild type strain. *mig-6* was identified as highly expressed in *kpc-1* mutants compared to controls and PVD-specific rescued animals. Even though depletion of *mig-6* using feeding RNAi protocols in *kpc-1* mutant animals starting at the L1 larva stage did not suppressed aspects of the mutant phenotype, depletion in control animals under the same conditions produced an striking meandering phenotype for PVD 1° dendrite.

QUANTIFICATION AND STATISTICAL ANALYSIS—All quantitative raw data is shown in Data S1. Statistical tests were applied as described in each legend. Specifically, we used the Fisher test to compare proportions in ablation experiments. For all other proportions, statistical significance was calculated using the z test with Bonferroni correction for multiple comparisons where applicable. An unpaired *t* test was used to compare the proximity index between pairs of neuronal processes. Non-parametric Kruskal-Wallis was used to assess significance in Figure 3B. For RNAi knockdown experiments, one-way ANOVA was used for comparisons with Sidak's correction using the Prism7 Statistical Software suite from (GraphPad). Statistical significance is indicated as ns, not significant; *$p \leq 0.05$; **$p \leq 0.01$; ***$p \leq 0.001$ and ****$p \leq 0.0001$.

Supplementary Material

Refer to Web version on PubMed Central for supplementary material.

ACKNOWLEDGMENTS

We thank Chun-Hao Chen and Chun-Liang Pan for sharing unpublished observations and C. Bénard, T. Goncalves, J. Hébert, R. Pocock, C. Rubin, Y. Salzberg, S. Cook, R. Christensen, and members of the Bülow laboratory for comments on the manuscript or discussions during the course of this work. We thank the CGC for strains (funded by NIH Office of Research Infrastructure Programs, P40OD010440) and O. Hobert, K.R. Norman, W. Wadsworth, D. Miller III, C. Bénard, C. Díaz-Balzac, and J. Culotti for reagents. This work was supported by grants from the National Institute of Health (R01NS096672 to H.E.B.; T32GM007491 to C.J.S.; R24OD010943 to D.H.; P30CA013330 to the AIF) and the Binational Science Foundation (#2013188 to H.E.B). Electron microscopy in the Hall lab was supported by NIH grant P30HD071593. N.J.R.S. is the recipient of a Colciencias-Fulbright Fellowship, and H.E.B. is an Irma T. Hirschl/Monique Weill-Caulier research fellow.

REFERENCES

Albeg A, Smith CJ, Chatzigeorgiou M, Feitelson DG, Hall DH, Schafer WR, Miller DM, 3rd, and Treinin M (2011). C. elegans multi-dendritic sensory neurons: morphology and function. Mol. Cell. Neurosci 46, 308–317. [PubMed: 20971193]

Altman J, and Anderson WJ (1972). Experimental reorganization of the cerebellar cortex. I. Morphological effects of elimination of all microneurons with prolonged x-irradiation started at birth. J. Comp. Neurol 146, 355–405. [PubMed: 5086676]

Altun ZF, Chen B, Wang ZW, and Hall DH (2009). High resolution map of Caenorhabditis elegans gap junction proteins. Dev. Dyn 238, 1936–1950. [PubMed: 19621339]

Arce EA, Bennett-Clarke CA, Mooney RD, and Rhoades RW (1992). Synaptic organization of the serotoninergic input to the superficial gray layer of the hamster's superior colliculus. Synapse 11, 67–75. [PubMed: 1604424]

Bhattacharya A, Aghayeva U, Berghoff E, and Hobert O (2019). Plasticity of the electrical connectome of C. elegans. Cell 10.1016/j.cell.2018.12.024.

Bülow HE, Berry KL, Topper LH, Peles E, and Hobert O (2002). Heparan sulfate proteoglycan-dependent induction of axon branching and axon misrouting by the Kallmann syndrome gene kal-1. Proc. Natl. Acad. Sci. U S A 99, 6346–6351. [PubMed: 11983919]

Chatzigeorgiou M, Yoo S, Watson JD, Lee WH, Spencer WC, Kindt KS, Hwang SW, Miller DM, 3rd, Treinin M, Driscoll M, et al. (2010). Specific roles for DEG/ENaC and TRP channels in touch and thermosensation in C. elegans nociceptors. Nat. Neurosci 13, 861–868. [PubMed: 20512132]

Chen CH, Hsu HW, Chang YH, and Pan CL (2019). Adhesive L1CAM-Robo signaling aligns growth cone F-actin dynamics to promote axon-dendrite fasciculation in C. elegans. Dev. Cell 48 Published online December 13, 2018 10.1016/j.devcel.2018.10.028.

Constance WD, Mukherjee A, Fisher YE, Pop S, Blanc E, Toyama Y, and Williams DW (2018). Neurexin and neuroligin-based adhesion complexes drive axonal arborisation growth independent of synaptic activity. Elife 7.

Díaz-Balzac CA, Lázaro-Peña MI, Ramos-Ortiz GA, and Bülow HE (2015). The adhesion molecule KAL-1/anosmin-1 regulates neurite branching through a SAX-7/L1CAM-EGL-15/FGFR receptor complex. Cell Rep 11, 1377–1384. [PubMed: 26004184]

Díaz-Balzac CA, Rahman M, Lázaro-Peña MI, Martin Hernandez LA, Salzberg Y, Aguirre-Chen C, Kaprielian Z, and Bülow HE (2016). Muscle- and skin-derived cues jointly orchestrate patterning of somatosensory dendrites. Curr. Biol 26, 2379–2387. [PubMed: 27451901]

Dickinson DJ, Pani AM, Heppert JK, Higgins CD, and Goldstein B (2015). Streamlined genome engineering with a self-excising drug selection cassette. Genetics 200, 1035–1049. [PubMed: 26044593]

Dominici C, Moreno-Bravo JA, Puiggros SR, Rappeneau Q, Rama N, Vieugue P, Bernet A, Mehlen P, and Chédotal A (2017). Floor-plate-derived netrin-1 is dispensable for commissural axon guidance. Nature 545, 350–354. [PubMed: 28445456]

Dong X, Liu OW, Howell AS, and Shen K (2013). An extracellular adhesion molecule complex patterns dendritic branching and morphogenesis. Cell 155, 296–307. [PubMed: 24120131]

Dong X, Shen K, and Bülow HE (2015). Intrinsic and extrinsic mechanisms of dendritic morphogenesis. Annu. Rev. Physiol 77, 271–300. [PubMed: 25386991]

Fredens J, Engholm-Keller K, Giessing A, Pultz D, Larsen MR, HØjrup P, MØller-Jensen J, and Færgeman NJ (2011). Quantitative proteomics by amino acid labeling in C. elegans. Nat. Methods 8, 845–847. [PubMed: 21874006]

Fry AL, Laboy JT, and Norman KR (2014). VAV-1 acts in a single interneuron to inhibit motor circuit activity in Caenorhabditis elegans. Nat. Commun 5, 5579. [PubMed: 25412913]

Gendrel M, Atlas EG, and Hobert O (2016). A cellular and regulatory map of the GABAergic nervous system of C. elegans. Elife 5, 10.7554/eLife.17686.

Ghiretti AE, and Paradis S (2014). Molecular mechanisms of activity-dependent changes in dendritic morphology: role of RGK proteins. Trends Neurosci 37, 399–407. [PubMed: 24910262]

Gilleard JS, Barry JD, and Johnstone IL (1997). cis regulatory requirements for hypodermal cell-specific expression of the Caenorhabditis elegans cuticle collagen gene dpy-7. Mol. Cell. Biol 17, 2301–2311. [PubMed: 9121480]

Greenough WT, and Chang FL (1988). Dendritic pattern formation involves both oriented regression and oriented growth in the barrels of mouse somatosensory cortex. Brain Res 43, 148–152.

Hall DH (1995). Elctron microscopy and three-dimensional image reconstruction. Methods Cell Biol 48, 395–436. [PubMed: 8531736]

Hall DH, Hartwieg E, and Nguyen KCQ (2012). Modern electron microscopy methods for C. elegans. Methods Cell Biol 107, 93–149. [PubMed: 22226522]

Harterink M, da Silva ME, Will L, Turan J, Ibrahim A, Lang AE, van Battum EY, Pasterkamp RJ, Kapitein LC, Kudryashov D, et al. (2017). DeActs: genetically encoded tools for perturbing the actin cytoskeleton in single cells. Nat. Methods 14, 479–482. [PubMed: 28394337]

Hayashi S, Inoue Y, Kiyonari H, Abe T, Misaki K, Moriguchi H, Tanaka Y, and Takeichi M (2014). Protocadherin-17 mediates collective axon extension by recruiting actin regulator complexes to interaxonal contacts. Dev. Cell 30, 673–687. [PubMed: 25199687]

Hiramoto M, Hiromi Y, Giniger E, and Hotta Y (2000). The Drosophila Netrin receptor Frazzled guides axons by controlling Netrin distribution. Nature 406, 886–889. [PubMed: 10972289]

Itoh K, Cheng L, Kamei Y, Fushiki S, Kamiguchi H, Gutwein P, Stoeck A, Arnold B, Altevogt P, and Lemmon V (2004). Brain development in mice lacking L1-L1 homophilic adhesion. J. Cell Biol 165, 145–154. [PubMed: 15067019]

Iwasato T, Datwani A, Wolf AM, Nishiyama H, Taguchi Y, Tonegawa S, Knöpfel T, Erzurumlu RS, and Itohara S (2000). Cortex-restricted disruption of NMDAR1 impairs neuronal patterns in the barrel cortex. Nature 406, 726–731. [PubMed: 10963597]

Jafari G, Burghoorn J, Kawano T, Mathew M, Morck C, Axang C, Ailion M, Thomas JH, Culotti JG, Swoboda P, et al. (2010). Genetics of extracellular matrix remodeling during organ growth using the Caenorhabditis elegans pharynx model. Genetics 186, 969–982. [PubMed: 20805556]

Jang H, Levy S, Flavell SW, Mende F, Latham R, Zimmer M, and Bargmann CI (2017). Dissection of neuronal gap junction circuits that regulate social behavior in Caenorhabditis elegans. Proc. Natl. Acad. Sci. U S A 114,E1263–E1272. [PubMed: 28143932]

Kamiyama D, McGorty R, Kamiyama R, Kim MD, Chiba A, and Huang B (2015). Specification of dendritogenesis site in Drosophila aCC motoneuron by membrane enrichment of Pak1 through Dscam1. Dev. Cell 35, 93–106. [PubMed: 26460947]

Kawano T, Zheng H, Merz DC, Kohara Y, Tamai KK, Nishiwaki K, and Culotti JG (2009). C. elegans mig-6 encodes papilin isoforms that affect distinct aspects of DTC migration, and interacts genetically with mig-17 and collagen IV. Development 136, 1433–1442. [PubMed: 19297413]

Kim B, and Emmons SW (2017). Multiple conserved cell adhesion protein interactions mediate neural wiring of a sensory circuit in C. elegans. Elife 6.

Kim E, Sun L, Gabel CV, and Fang-Yen C (2013). Long-term imaging of Caenorhabditis elegans using nanoparticle-mediated immobilization. PLoS One 8, e53419. [PubMed: 23301069]

Kramerova IA, Kawaguchi N, Fessler LI, Nelson RE, Chen Y, Kramerov AA, Kusche-Gullberg M, Kramer JM, Ackley BD, Sieron AL, et al. (2000). Papilin in development; a pericellular protein with a homology to the ADAMTS metalloproteinases. Development 127, 5475–5485. [PubMed: 11076767]

Lefebvre JL, Sanes JR, and Kay JN (2015). Development of dendritic form and function. Annu. Rev. Cell Dev. Biol 31, 741–777. [PubMed: 26422333]

Liang X, Dong X, Moerman DG, Shen K, and Wang X (2015). Sarcomeres pattern proprioceptive sensory dendritic endings through UNC-52/perlecan in C. elegans. Dev. Cell 33, 388–400. [PubMed: 25982673]

Liu X, Wang X, and Shen K (2016). Receptor tyrosine phosphatase CLR-1 acts in skin cells to promote sensory dendrite outgrowth. Dev. Biol 413, 60–69. [PubMed: 26968353]

Mohammadi A, Byrne Rodgers J, Kotera I, and Ryu WS (2013). Behavioral response of Caenorhabditis elegans to localized thermal stimuli. BMC Neurosci 14, 66. [PubMed: 23822173]

Nath RD, Chow ES, Wang H, Schwarz EM, and Sternberg PW (2016). C. elegans stress-induced sleep emerges from the collective action of multiple neuropeptides. Curr. Biol 26, 2446–2455. [PubMed: 27546573]

Nonet ML, Staunton JE, Kilgard MP, Fergestad T, Hartwieg E, Horvitz HR, Jorgensen EM, and Meyer BJ (1997). Caenorhabditis elegans rab-3 mutant synapses exhibit impaired function and are partially depleted of vesicles. J. Neurosci 17, 8061–8073. [PubMed: 9334382]

Oren-Suissa M, Hall DH, Treinin M, Shemer G, and Podbilewicz B (2010). The fusogen EFF-1 controls sculpting of mechanosensory dendrites. Science 328, 1285–1288. [PubMed: 20448153]

Owens DF, and Kriegstein AR (2002). Is there more to GABA than synaptic inhibition? Nat. Rev. Neurosci 3, 715–727. [PubMed: 12209120]

Peng YR, Tran NM, Krishnaswamy A, Kostadinov D, Martersteck EM, and Sanes JR (2017). Satb1 regulates Contactin 5 to pattern dendrites of a mammalian retinal ganglion cell. Neuron 95, 869–883.e6. [PubMed: 28781169]

Pocock R, Bénard CY, Shapiro L, and Hobert O (2008). Functional dissection of the C. elegans cell adhesion molecule SAX-7, a homologue of human L1. Mol. Cell. Neurosci 37, 56–68. [PubMed: 17933550]

Pujol N, Torregrossa P, Ewbank JJ, and Brunet JF (2000). The homeodomain protein CePHOX2/CEH-17 controls antero-posterior axonal growth in C. elegans. Development 127, 3361–3371. [PubMed: 10887091]

Rajan I, and Cline HT (1998). Glutamate receptor activity is required for normal development of tectal cell dendrites in vivo. J. Neurosci 18, 7836–7846. [PubMed: 9742152]

Salzberg Y, Díaz-Balzac CA, Ramirez-Suarez NJ, Attreed M, Tecle E, Desbois M, Kaprielian Z, and Bülow HE (2013). Skin-derived cues control arborization of sensory dendrites in Caenorhabditis elegans. Cell 155, 308–320. [PubMed: 24120132]

Salzberg Y, Ramirez-Suarez NJ, and Bülow HE (2014). The proprotein convertase KPC-1/furin controls branching and self-avoidance of sensory dendrites in Caenorhabditis elegans. PLoS Genet 10, e1004657. [PubMed: 25232734]

Sasakura H, Inada H, Kuhara A, Fusaoka E, Takemoto D, Takeuchi K, and Mori I (2005). Maintenance of neuronal positions in organized ganglia by SAX-7, a Caenorhabditis elegans homologue of L1. EMBO J 24, 1477–1488. [PubMed: 15775964]

Schiavo GG, Benfenati F, Poulain B, Rossetto O, de Laureto PP, DasGupta BR, and Montecucco C (1992). Tetanus and botulinum-B neurotoxins block neurotransmitter release by proteolytic cleavage of synaptobrevin. Nature 359, 832–835. [PubMed: 1331807]

Schmidt ERE, Brignani S, Adolfs Y, Lemstra S, Demmers J, Vidaki M, Donahoo AS, LillevÄli K, Vasar E, Richards LJ, et al. (2014). Subdomain-mediated axon-axon signaling and chemoattraction cooperate to regulate afferent innervation of the lateral habenula. Neuron 83, 372–387. [PubMed: 25033181]

Siegenthaler D, Enneking EM, Moreno E, and Pielage J (2015). L1CAM/neuroglian controls the axon-axon interactions establishing layered and lobular mushroom body architecture. J. Cell Biol 208, 1003–1018. [PubMed: 25825519]

Silletti S, Mei F, Sheppard D, and Montgomery AMP (2000). Plasmin-sensitive dibasic sequences in the third fibronectin-like domain of L1-cell adhesion molecule (CAM) facilitate homomultimerization and concomitant integrin recruitment. J. Cell Biol 149, 1485–1502. [PubMed: 10871287]

Sin WC, Haas K, Ruthazer ES, and Cline HT (2002). Dendrite growth increased by visual activity requires NMDA receptor and Rho GTPases. Nature 419, 475–480. [PubMed: 12368855]

Smith CJ, O'Brien T, Chatzigeorgiou M, Spencer WC, Feingold-Link E, Husson SJ, Hori S, Mitani S, Gottschalk A, Schafer WR, et al. (2013). Sensory neuron fates are distinguished by a transcriptional switch that regulates dendrite branch stabilization. Neuron 79, 266–280. [PubMed: 23889932]

Smith CJ, Watson JD, Spencer WC, O'Brien T, Cha B, Albeg A, Treinin M, and Miller DM, 3rd (2010). Time-lapse imaging and cell-specific expression profiling reveal dynamic branching and molecular determinants of a multi-dendritic nociceptor in C. elegans. Dev. Biol 345, 18–33. [PubMed: 20537990]

Smith CJ, Watson JD, VanHoven MK, Colón-Ramos DA, and Miller DM, 3rd (2012). Netrin (UNC-6) mediates dendritic self-avoidance. Nat. Neurosci 15, 731–737. [PubMed: 22426253]

Tang LTH, Díaz-Balzac CA, Rahman M, Ramirez-Suarez NJ, Salzberg Y, Lázaro-Peña MI, and Bülow HE (2018). TIAM-1/GEF can shape somatosensory dendrites independently of its GEF activity by regulating F-actin localization. bioRxiv, 347567, 10.1101/347567.

Tsalik EL, Niacaris T, Wenick AS, Pau K, Avery L, and Hobert O (2003). LIM homeobox gene-dependent expression of biogenic amine receptors in restricted regions of the C. elegans nervous system. Dev Biol 263, 81–102. [PubMed: 14568548]

Uhlrich DJ, Manning KA, and Pienkowski TP (1993). The histaminergic innervation of the lateral geniculate complex in the cat. Vis. Neurosci 10, 225–235. [PubMed: 8485087]

Varadarajan SG, Kong JH, Phan KD, Kao TJ, Panaitof SC, Cardin J, Eltzschig H, Kania A, Novitch BG, and Butler SJ (2017). Netrin1 produced by neural progenitors, not floor plate cells, is required for axon guidance in the spinal cord. Neuron 94, 790–799.e3. [PubMed: 28434801]

Wang X, Kweon J, Larson S, and Chen L (2005). A role for the C. elegans L1CAM homologue lad-1/sax-7 in maintaining tissue attachment. Dev. Biol 284,273–291. [PubMed: 16023097]

Weinberg P, Berkseth M, Zarkower D, and Hobert O (2018). Sexually dimorphic unc-6/Netrin expression controls sex-specific maintenance of synaptic connectivity. Curr. Biol 28, 623–629.e3. [PubMed: 29429615]

Wenick AS, and Hobert O (2004). Genomic cis-regulatory architecture and trans-acting regulators of a single interneuron-specific gene battery in C. elegans. Dev. Cell 6, 757–770. [PubMed: 15177025]

White JG, Southgate E, Thomson JN, and Brenner S (1986). The structure of the nervous system of the nematode *Caenorhabditis elegans*. Philos. Trans. R. Soc. B Biol. Sci 314, 1–340.

Wong ROL, and Ghosh A (2002). Activity-dependent regulation of dendritic growth and patterning. Nat. Rev. Neurosci 3, 803–812. [PubMed: 12360324]

Wu Y, Ghitani A, Christensen R, Santella A, Du Z, Rondeau G, Bao Z, Colon-Ramos D, and Shroff H (2011). Inverted selective plane illumination microscopy (iSPIM) enables coupled cell identity lineaging and neurodevelop-mental imaging in Caenorhabditis elegans. Proc. Natl. Acad. Sci. U S A 108, 17708–17713. [PubMed: 22006307]

Yanowitz JL, Shakir MA, Hedgecock E, Hutter H, Fire AZ, and Lundquist EA (2004). UNC-39, the C. elegans homolog of the human myotonic dystrophy-associated homeodomain protein Six5, regulates cell motility and differentiation. Dev. Biol 272, 389–402. [PubMed: 15282156]

Zahn TR, Angleson JK, MacMorris MA, Domke E, Hutton JF, Schwartz C, and Hutton JC (2004). Dense core vesicle dynamics in Caenorhabditis elegans neurons and the role of kinesin UNC-104. Traffic 5, 544–559. [PubMed: 15180830]

Zhou S, and Chen L (2011). Neural integrity is maintained by dystrophin in C. elegans. J. Cell Biol 192, 349–363. [PubMed: 21242290]

Zhou Z, Hong EJ, Cohen S, Zhao WN, Ho HH, Schmidt L, Chen WG, Lin Y, Savner E, Griffith EC, et al. (2006). Brain-specific phosphorylation of MeCP2 regulates activity-dependent bdnf transcription, dendritic growth, and spine maturation. Neuron 52, 255–269. [PubMed: 17046689]

Zou W, Dong X, Broederdorf TR, Shen A, Kramer DA, Shi R, Liang X, Miller DM, 3rd, Xiang YK, Yasuda R, et al. (2018). A dendritic guidance receptor complex brings together distinct actin regulators to drive efficient F-actin assembly and branching. Dev. Cell 45, 362–375.e3. [PubMed: 29738713]

Zou W, Shen A, Dong X, Tugizova M, Xiang YK, and Shen K (2016). A multi-protein receptor-ligand complex underlies combinatorial dendrite guidance choices in C. elegans. Elife 5 10.7554/eLife.18345.

Highlights

- ALA axons control guidance and extension of PVD dendrites independently of activity
- MIG-6/Papilin and the Netrin pathway shape PVD dendrites through ALA axon patterning
- SAX-7/L1CAM acts with Menorin to promote PVD 1° dendrite extension along ALA axons
- SAX-7/L1 CAM maintains ALA-PVD fasciculation post-embryonically

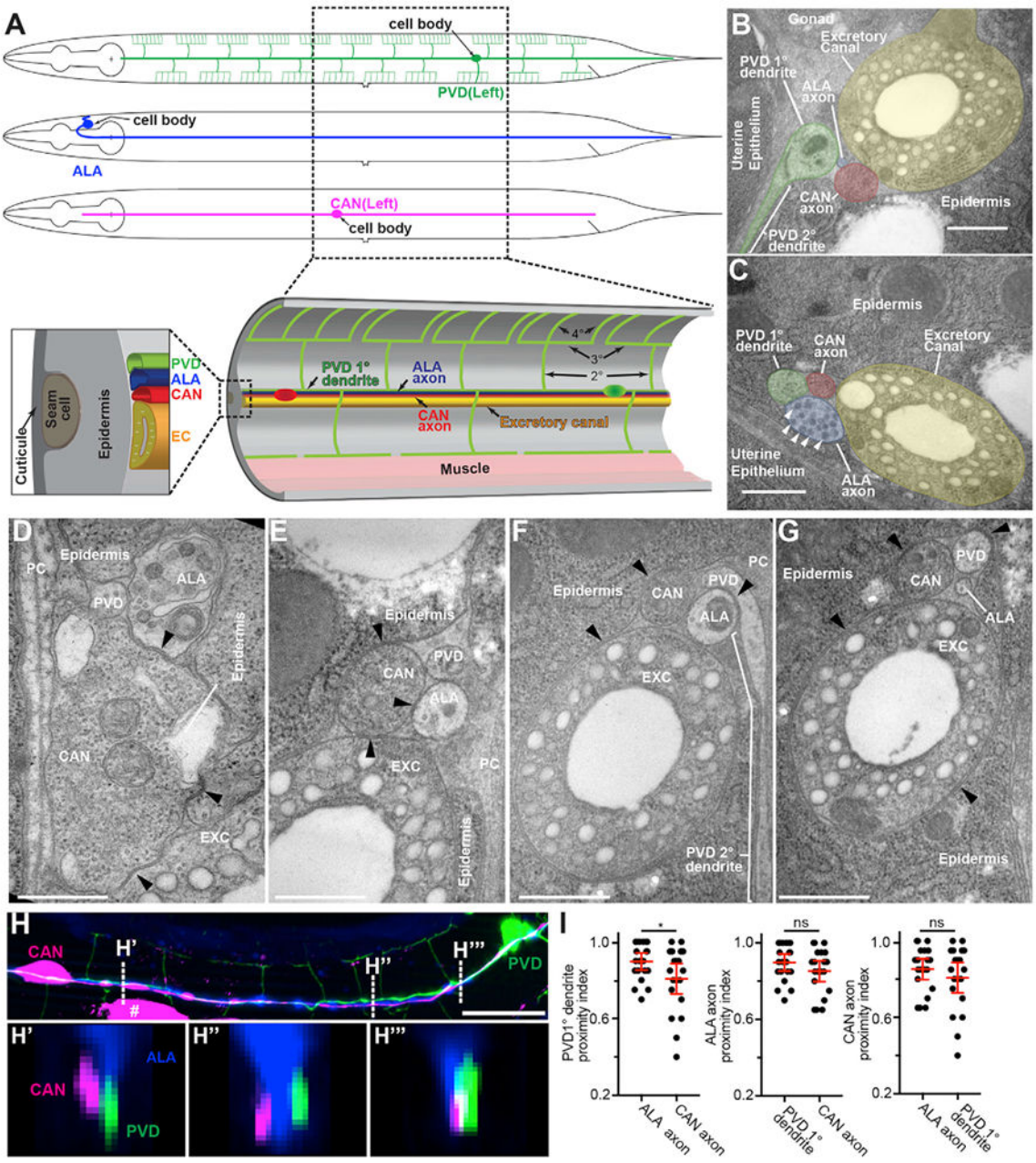

Figure 1. Processes in the Lateral Nerve Tract Present Preferential Association and Are Enriched in Electrical Synapses

(A) Schematics of PVD (green), ALA (blue), CAN (red) neurons, and the excretory canal (yellow) in adult animals.

(B and C) TEM image of lateral nerve tract cross-sections. A 2° branch for PVD is shown in (B). The presence of dense core vesicles in an ALA axon in (C) is indicated by arrowheads. Color code as in (A). Scale bar, 0.5 μm.

(D-G) TEM micrographs showing electrical synapses between the processes of ALA, CAN and PVD, and surrounding tissues. (D) A mid-body section where the right-side ALA axon

(identified by large dense core vesicles and a large smooth ER compartment) and a PVD dendrite are enveloped by epidermis. Arrowheads show gap junctions in CAN processes close to its cell body, contacting with either epidermis or the excretory canal (EXC). PC, pseudocoelum. Additional examples of gap junctions (arrowheads) between members of the left lateral nerve are shown in (E)–(G). Scale bar, 0.5 μm in (D), (F), and (G). Scale bar, 0.33 μm in (E).

(H) Fluorescent image showing the processes of ALA *(dzEx1766),* CAN (otIs33), and the PVD 1° dendrite *(dzIs53)* using the same color code as in (A). Scale bar, 20 μm. The location of optical cross sections in the lateral nerve tract are indicated by dashed lines with corresponding cross sections shown below (H', H" or H"').

(I) Pairwise comparisons of neurite proximity for the PVD 1° dendrite, ALA axon, and the CAN process. For proximity index calculation see STAR Methods. Statistical significance is indicated as *p = 0.0452; ns, not significant. Error bars represent 95% CI. n = 400 orthogonal optical sections (20 sections per animal). See also Tables S1 and S2; Figures S1 and S6.

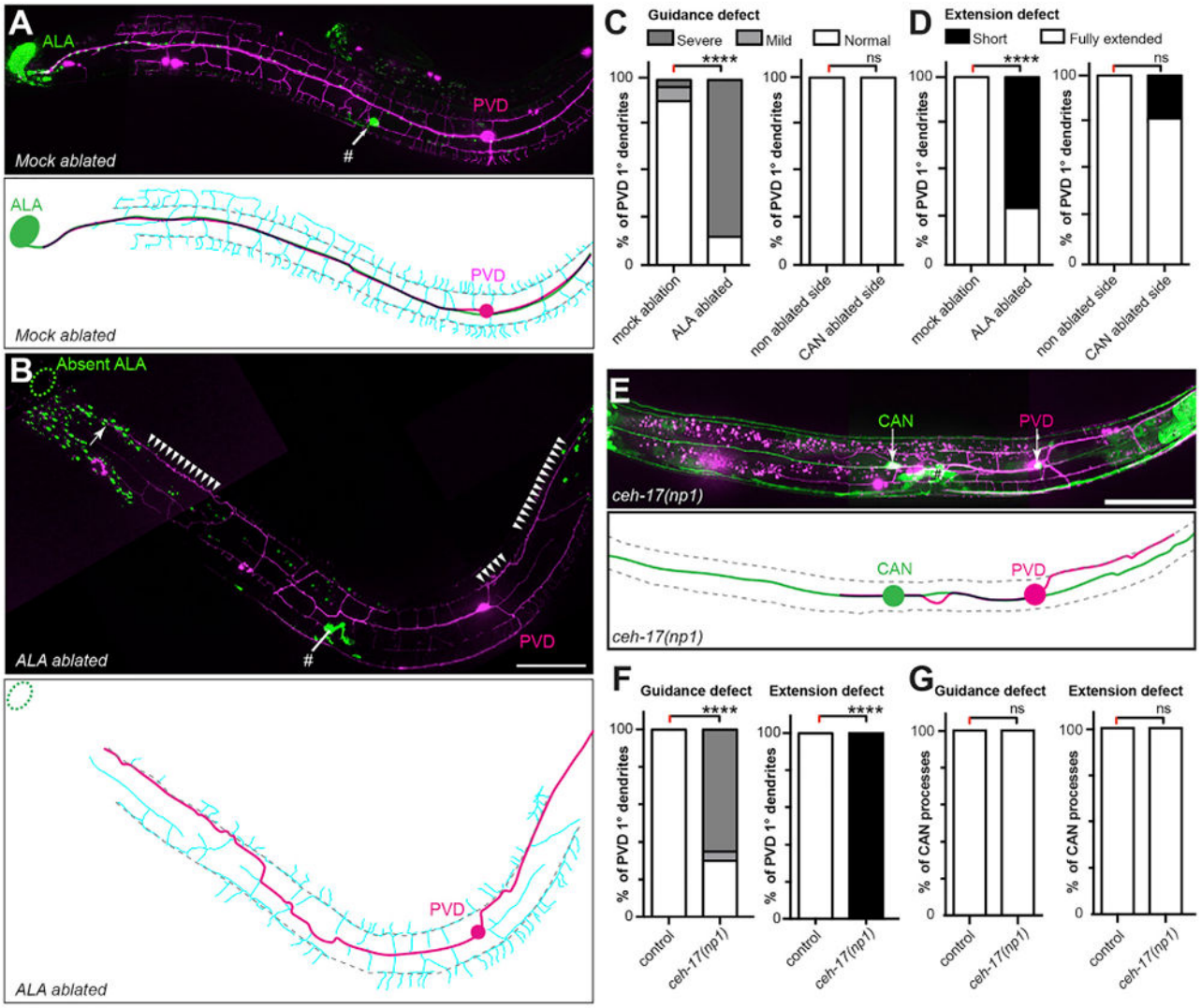

Figure 2. The ALA Neuron Promotes Guidance and Extension of the PVD 1° Dendrite

(A and B) Composite fluorescent images (upper panels) and corresponding schematics (bottom panels) of mock-ablated (A) or ALA L1-ablated animals (B) at the L4/young adult stage. In all schematics (A, B, and E), visual overlap between PVD (magenta, *dzIs53)* dendrites and ALA (green, *inIs181)* or CAN (green, *otIs33)* processes is indicated in black; sublateral lines (where 3° branches are located) are shown as gray dashed lines and menorahs in cyan where applicable. In (B), an arrow indicates the short and arrowheads the misguided PVD 1° dendrite, whereas a dotted circle indicates the location of the ablated ALA soma. Anterior is to the left and ventral to the bottom. (#) indicates fluorescence in the vulva region in all images. Scale bar, 50 μm.

(C and D) Quantification of PVD 1° dendrite guidance (C) and extensions (D) defects in animals as indicated. In (C), (F), and (G), a meandering PVD 1° dendrite reaching the sublateral lines was classified as a severe guidance defect and a 1° dendrite meandering between the sublateral lines was classified as mild guidance defect. Data are presented as

percentage of animals with normal, mild, or severe phenotypes. In (D), a short PVD 1° dendrite is defined as a process unable to reach the posterior bulb of the pharynx. For ALA ablations (n = 13), a PVD 1° dendrite from mock-ablated animals (n = 26) was used as control. For CAN ablations (n = 12), the PVD 1° dendrite from the contralateral side, was used as control.

(E) Composite fluorescent image (upper panel) and corresponding schematics (bottom panel) of *ceh-17(np1)* mutant animals with CAN labeled in green *(otIs33)* and PVD in magenta *(dzIs53).* Note the unaffected CAN processes and the short and mispositioned PVD 1° dendrite. Scale bar, 50 μm.

(F and G) Quantification of PVD 1° (F) and CAN (G) guidance and extension defects in the genotypes indicated. Data are presented as percentage of animals with defective PVD 1° dendrites or CAN processes (F) n = 24 (PVD) and (G) n = 25 (CAN) for mutants; n = 102 for controls). Guidance defects for PVD 1° dendrites and CAN processes were defined as for PVD in (C); PVD extension defects as in (D) and CAN processes were considered short when either or both were unable to reach the posterior bulb of the pharynx (anterior process) or the anus (posterior process), respectively. For statistical purposes, severe and mild phenotypes were pooled (F and G).

**** $p \leq 0.0001$ by Fisher's test in (C), (D), and (F). ns, not significant. See also Tables S1 and S2, Figures S1 and S6.

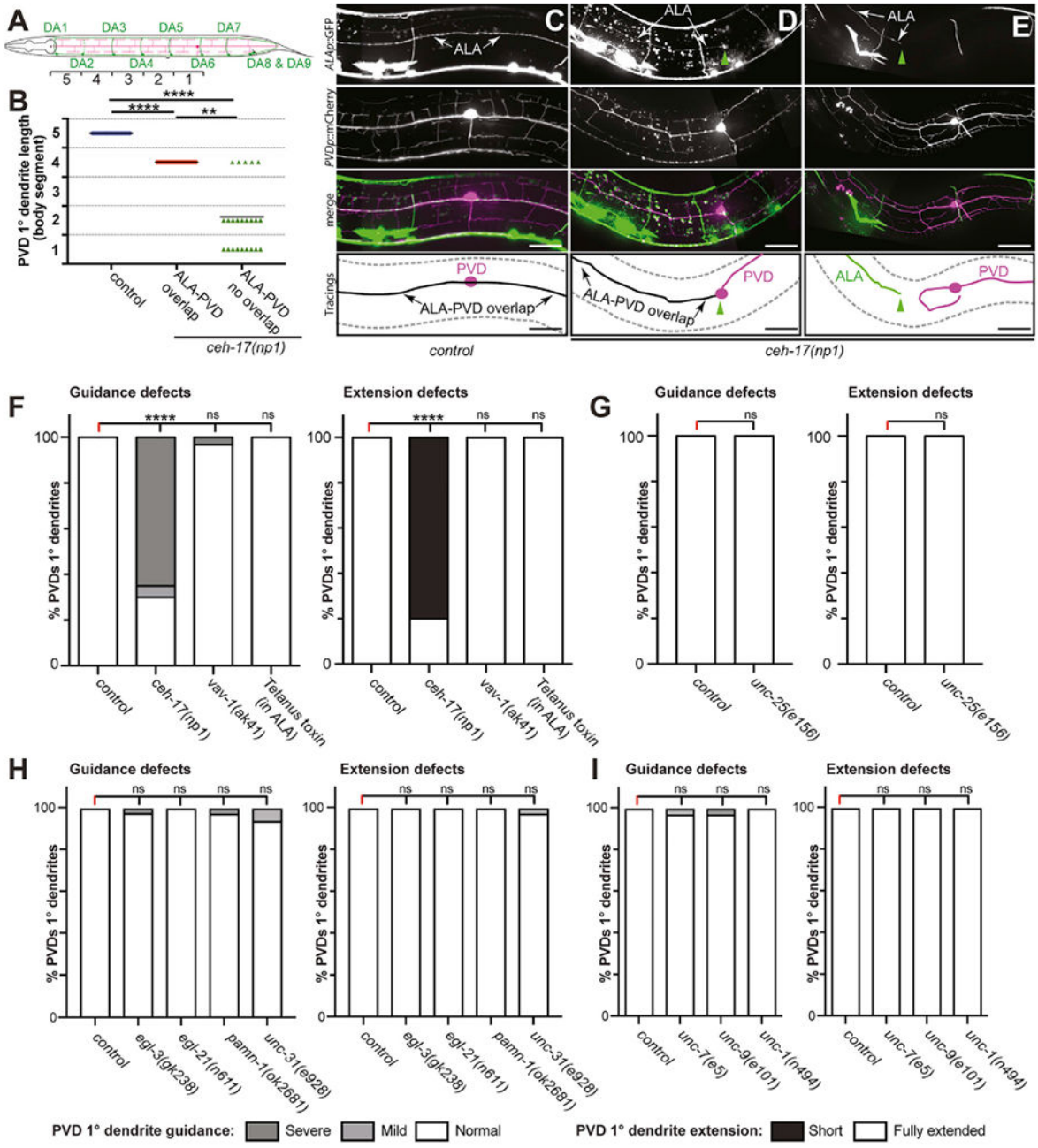

Figure 3. ALA Patterns PVD 1° Dendrites Independently of Activity

(A) Schematic of an animal showing PVD (magenta) and DA motor neurons (green). DA1 to DA6 motor neurons were used as landmarks to define five body segments that were used to categorize anterior PVD 1° dendrite extension in mutants and controls.

(B) Quantification of PVD 1° dendrite extension defects in control and *ceh-17(np1)* mutant animals using the body segments described in (A). Blue, red, and green triangles indicate animals with complete (control animals), partial, and no ALA and PVD overlap, respectively. n = 24 for each group.

(C–E) Examples of lateral composite fluorescent micrographs and corresponding tracings of animals described in (B) control animals, (C) A representative *ceh-17* mutant animal from the overlapping group, and (D) a *ceh-17* mutant animal from the non-overlapping group (E). In all images, the PVD 1° dendrite was considered the thicker process running along the anterior-posterior axis of the animal. Green arrowheads indicate the tip of the truncated ALA axon in *ceh-17* mutants. Visual overlap between ALA axons (green, *bgEx21)* and PVD 1° dendrites (magenta, *dzIs53)* in schematics are indicated in black. Scale bar, 20 μm.
(F–I) Quantification of PVD anterior 1° guidance (left) and PVD 1° dendrite extension defects (right) in the genotypes indicated. Data for *ceh-17* is identical as in Figure 2F and is shown for comparison only. (F, n = 20–35; G, n = 30; H, n = 29–32; I, n = 25). For (F–I) PVD 1° guidance defects were scored as in Figure 2C and PVD 1° dendrite outgrowth was scored as in Figure 2D. Statistical significance was computed using the Kruskal-Wallis test with significance adjusted for multiple comparisons (B) or the Z score test (F–I).
ns, not significant, ** $p \leq 0.01$, **** $p \leq 0.0001$. See also Table S2, Figure S6.

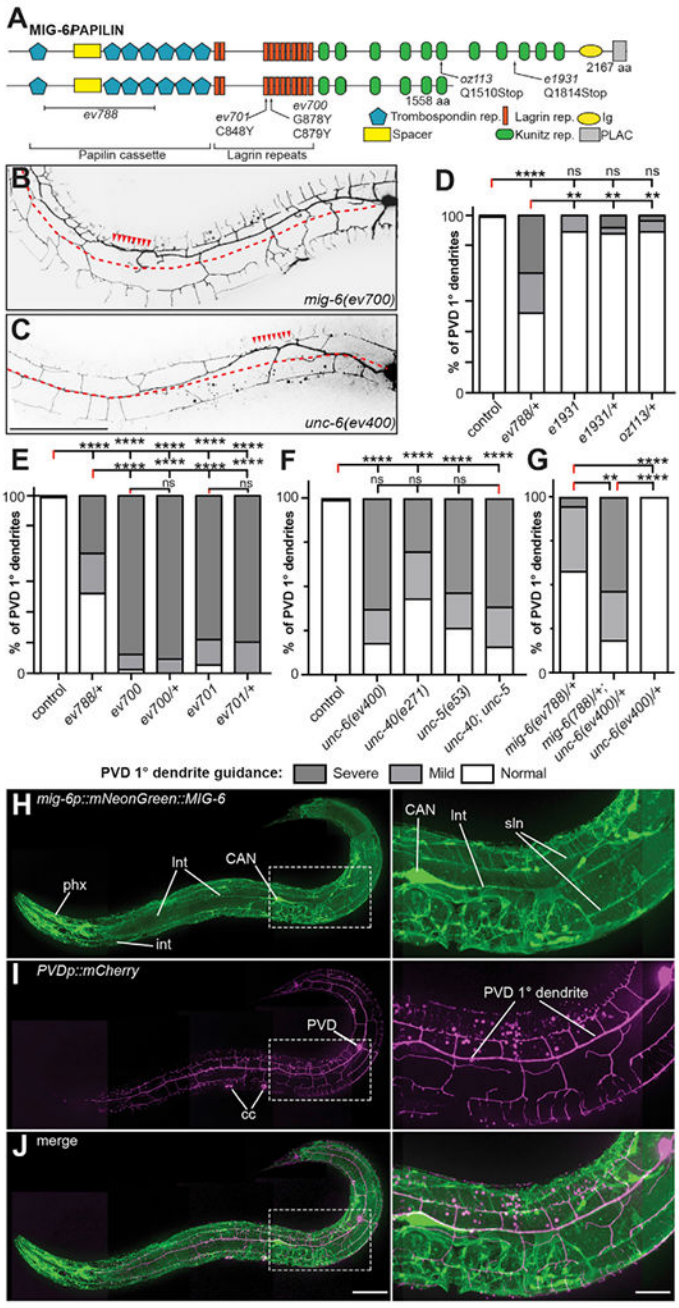

Figure 4. MIG-6/Papilin and the Netrin Pathway Position the PVD 1° Dendrite at the Lateral Mid-line

(A) Schematic of MIG-6/Papilin with alleles and protein domains.

(B and C) Composite fluorescent images of *mig-6(ev700)* (B) and *unc-6(ev400)* (C) mutant animals. A red dashed line indicates the normal position of the PVD 1° dendrite and red arrowheads show misplacement of the 1° dendrite. Scale bar, 50 μm. (D–G) Quantification of PVD 1° guidance defects in the genotypes indicated. Data are presented as percentage of animals with normal, mild, or severe phenotypes as in Figure 2C (n = 29–103). All animals in (G) carried one copy of the *dpy-11(e224)* allele. Statistical significance was computed

using the Z score test with Bonferroni correction: ns, not significant; **p ≤ 0.01; ****p ≤ 0.0001.

(H–J) Composite fluorescent images of a 1-day-old wild-type animal transgenically expressing a mNeonGreen::MIG-6S fusion driven by the *mig-6* $p_{(5.4kb)}$ promoter. The PVD neuron is visualized by a cytoplasmic marker *(dzIs53,* magenta). A merged image of (H) and (I) is shown in (J). Images on the right are magnifications of insets on the left as indicated. phx (pharynx), lnt (lateral nerve tract), sln (sublateral nerve cord), and int (intestine). Scale bar, 50 μm for left and 20 μm for right panels. Similar localization of mNeonGreen::MIG-6S is observed in rescue experiments (see Figure S3).

See also Table S2; Figures S2, S3, and S6.

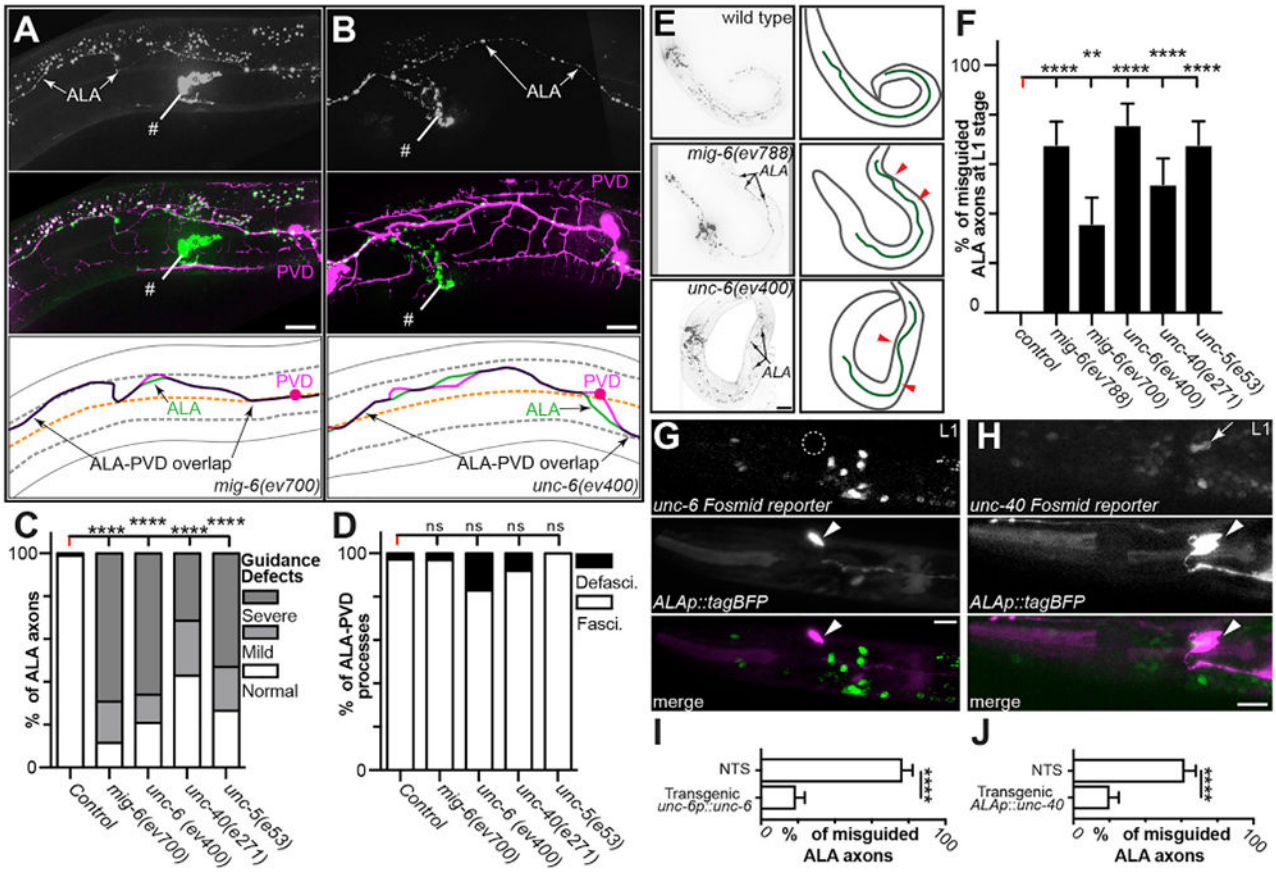

Figure 5. ALA Axonal Defects Predict PVD 1° Guidance Defects

(A and B) Composite fluorescent images of *mig-6(ev700)* (A) and *unc-6(ev400)* (B) mutant animals showing the ALA axons alone (top panels) or a merged image between ALA (in green) and PVD (in magenta)(middle panel). A black line in the schematics (bottom panels) indicate overlap between the ALA axon and the PVD 1° dendrite. Dashed grey lines denote the location of PVD 3° dendrites. "#" in upper panels indicates fluorescence in the vulva region. Scale bar, 20 μm.

(C and D) Quantification of ALA axon guidance (C) and fasciculation (D) defects in the genotypes indicated (see also Table S2). Data are presented as percentage of animals with normal, mild, or severe phenotypes (C, n = 26–101) and with fasciculated or defasciculated lateral nerve tracts (D, n = 25–36). A separation of the PVD and ALA neurites for a distance of at least 20 μm along the lateral nerve cord was considered defective for fasciculation.

(E) Lateral fluorescent image of a *mig-6(ev700), unc-6(ev400),* and wild-type animals at the L1 stage (left) with schematics (right) showing the ALA axons in green. Guidance defects in ALA axons are indicated by red arrowheads. Scale bar, 20 μm.

(F) Quantification of ALA guidance defects in the genetic backgrounds as indicated. Data are represented as percentage of defective ALA axons ± SEP. A deviation of the ALA axon from the lateral midline was considered defective (n = 25).

(G and H) L1 animals carrying a nuclear *unc-6::YFP* (G, *otIs638,* top panel) or a nuclear *unc-40::nYFP* fosmid-based transcriptional reporter (H, *dzIs118,* top panel), a cytoplasmic marker for *ALAp::tagBFP (dzEx1823,* middle panels), and a merged image (bottom panels). A dashed circle shows the location of the ALA soma (G), an arrow the ALA nucleus (H), and arrowheads point to ALA cell somata (G and H). Scale bar, 20 μm.

(I and J) Quantification of transgenic rescue of ALA guidance defects using the *unc-6* genomic locus (I) or the *unc-40* cDNA driven by an ALA-specific promoter *(ida-1p)* (J). Data are represented as percentage of ALA axons with guidance defects ± SEP and are the composite of two independent transgenic lines for both (I and J). NTS, non-transgenic siblings.

Statistical significance was computed using the Z score test in (C), (D), (F), (I), and (J). ns, not significant; **p ≤ 0.01; ****p ≤ 0.0001. See also Table S2, Figure S6.

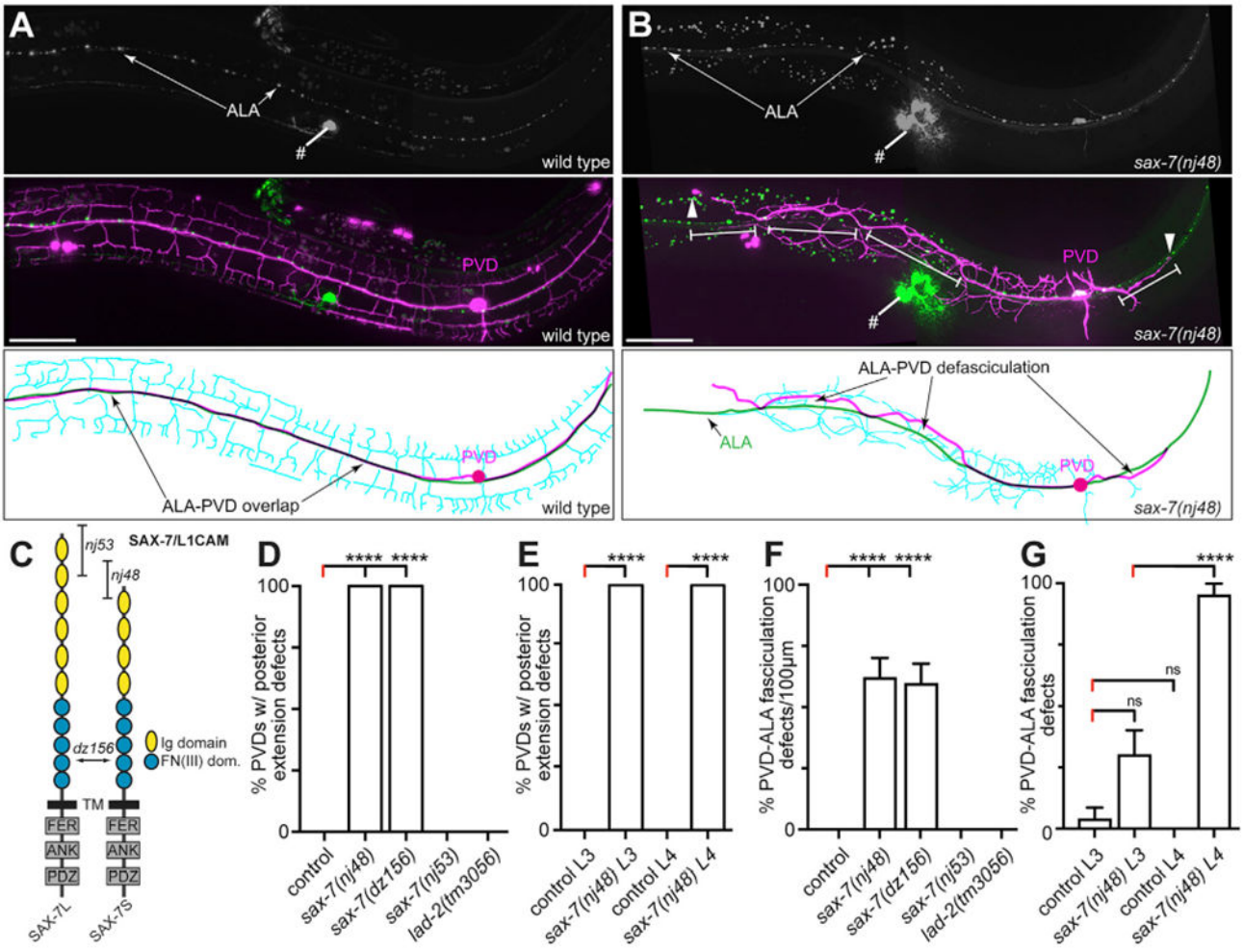

Figure 6. SAX-7/L1CAM Promotes PVD 1° Dendrite Extension and Maintains Axon-Dendritic Fasciculation

(A and B) Composite fluorescent images of ALA (top panels), ALA and PVD *(inIs181; dzis53* green and magenta, middle panels), and corresponding schematics (lower panels) of the genotypes indicated (B). In (B), segments of defasciculation are indicated by white brackets; arrowheads indicate anterior and posterior truncation of the PVD 1° branch. Visual overlap between ALA (green) and PVD (magenta) processes in schematics is indicated in black. (A) is a cropped version of Figure 2A and shown for comparison only. "#" indicates fluorescence in the vulva region. Scale bars, 50 µm.

(C) Schematic of the SAX-7/L1CAM proteins with protein domains, the extent of deletions *(nj48* & *nj53),* and the position of the *dz156* non-sense allele are indicated.

(D–G) Quantification of PVD 1° posterior extension (D and E) and PVD-ALA fasciculation defects (F and G) for the genotypes and ages as indicated (young adults unless noted otherwise: L3, L3 larval stage; L4, L4 larval stage). In (D) and (E), the percentage of PVD 1° dendrites shorter than 100 µm is shown (D, n = 50; E, n = 23). In (F) and (G) the percentage of defective PVD 1° dendrites ± SEP is shown. Separation of the PVD 1° dendrite from the ALA axon for at least 20 µm in the 100 µm segment immediately anterior

to the PVD soma (F) or along the total PVD 1° dendrite length (G) was considered defective (F, n = 40; G, n = 23). Statistical significance was computed using the Z-score: ns, not significant; ****$p \leq 0.0001$. See also Table S2; Figure S6.

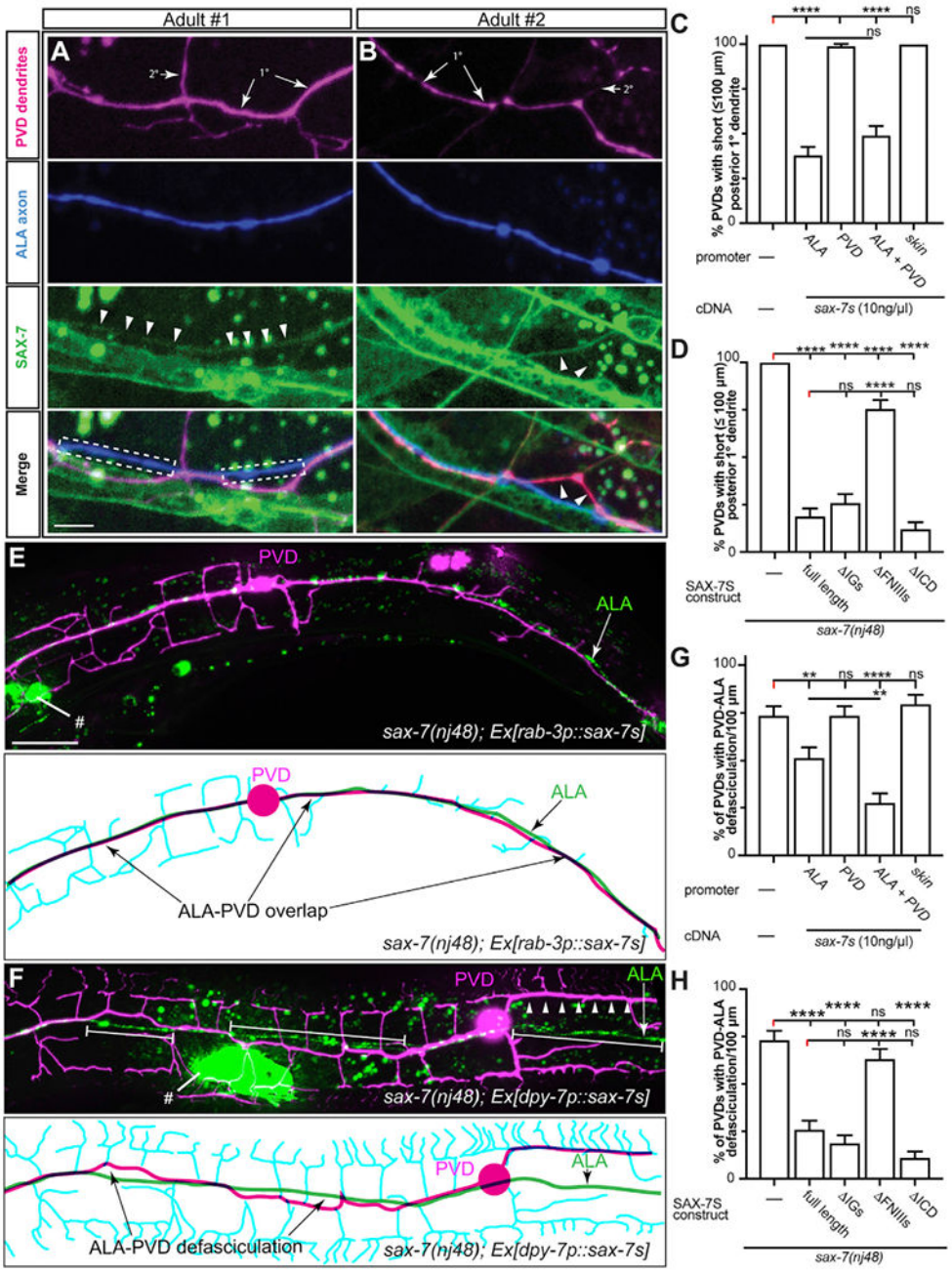

Figure 7. Neuronal SAX-7 Requires the FNIII Domains to Promote Dendrite Outgrowth and Fasciculation

(A and B) Single optical sections of two different two-day old adult wild-type animals showing PVD dendrites (magenta, *dzIs53),* ALA axons (blue, *dzEx1823),* and SAX-7::GFP localization (green, *ddIs290).* Note the SAX-7::GFP localization in the ALA process (A, arrowheads and corresponding dashed region in the merged image) and in a PVD 1° dendrite (B, arrowheads). Scale bar, 10 µm.

(C and D) Quantification of transgenic rescue of PVD 1° posterior extension defects in *sax-7(nj48)* mutants animals using cell-specific promoters (C: ALA: *ida-1p,* PVD: *ser-2p3s*,

skin: *dpy-7p)* or a pan-neuronal promoter (D: *unc-14p)* driving *sax-7S* cDNAs as indicated. At least 3 independent transgenic lines were generated per construct and the data combined (n = 30/line). Posterior extension and outgrowth defects were scored as in Figures 6D and 6F, respectively. Data for skin-specific expression is identical to Figure S4E and shown for comparison only. The percentage of PVD 1° dendrites with defects ± SEP is shown. Only one representative column of non-transgenic siblings is shown (–, non-transgenic siblings).
(E and F) Fluorescent images and schematics of *sax-7(nj48)* mutants expressing a *sax-7s* cDNA in neurons (E) or the epidermis (F). PVD and ALA visualized by *dzIs53* and *inIs181,* respectively. Defasciculated segments are indicated by white brackets; arrowheads indicate mislocalization of the PVD 1° dendrites and (#) indicates fluorescence in the vulva region. In schematics, visual overlap between ALA axon (green) and PVD 1° dendrite (magenta) are indicated in black and high-order branches in cyan. Anterior is to the left, dorsal is up. Scale bars, 20 μm.
(G and H) Quantification of transgenic rescue of PVD 1° defasciculation defects in *sax-7(nj48)* mutants animals using cell-specific promoters (ALA: *ida-1p,* PVD: *ser-2p*$_{3s}$*),* a pan-neuronal (D and H: *unc-14p),* or an epidermal promoter (*dpy-7p*) driving *sax-7S* cDNAs as indicated. At least 3 independent transgenic lines were generated per construct and the data combined (n = 30/line). The percentage of PVD 1° dendrites with defects ± SEP is shown. Only one representative column of non-transgenic siblings is shown (–, non-transgenic siblings).
Statistical significance was computed using the Z-score test: ns, not significant; ****p ≤ 0.0001. See also Figures S4 and S5.

KEY RESOURCES TABLE

REAGENT or RESOURCE	SOURCE	IDENTIFIER
Bacterial and Virus Strains		
E.coli: OP50	Caenorhabditis Genetics Center	OP50
Experimental Models: Organisms/Strains		
See Table S3		N/A
Oligonucleotides		
See Table S4		N/A
Recombinant DNA		
Plasmid: *pZH125 [mig-6p::mig-6s]*	Kawano et al., (2009)	N/A
Plasmid: *pZH135 [myo-3$_{prom}$::mig-6s]*	Kawano et al., (2009)	N/A
Plasmid: *pDD268*[mNeonGreen^SEC^3×Flag]	Dickinson et al. (2015)	N/A
Plasmid: *ida-1p$_{(12kb)}$::GFP*	A DNA fragment encoding 1182bp upstream of the ida-1 translational start site was cloned into *pPD95.75* using *Xba*I/*Xma*I.	N/A
Plasmid: *ida-1p$_{(1.2kb)}$*::GFP	A DNA fragment encoding 1182bp upstream of the ida-1 translational start site was cloned into *pPD95.75* using *Xba*I/*Xma*I.	N/A
Plasmid: *ceh-23p$_L$*::tagRFP	The promL DNA promoter fragment of *ceh-23* (Wenick and Hobert, 2004) was cloned into *myo-3p*::tagRFP using *Xba*I/*Xma*I.	N/A
Plasmid: *rab-3p::mig-6s*	The *mig-6s* coding and UTR region present in *ceh-23p$_L$::mig-6s* was cloned into a *rab-3p*::GFP plasmid using *Xma*I/*Apa*I replacing the tag fluorescent protein.	N/A
Plasmid: *ceh-23p$_L$::mig-6s*	*pZH125* was mutagenized at the −20 (c→t) and −16 (c→g) bp positions to introduce a *BspTI* site. The *mig-6s* DNA region downstream of the start site was cloned into a *ceh-23p$_L$*::tagRFP plasmid using *KpnI* or BsptI/*Apa*I and the adaptors cggtcgccacctaacataacc and ttaaggttatgttaggtggcgaccggtac	N/A
Plasmid: *ida-1p$_{(1.2kb)}$::mig-6s*	The *mig-6s* coding and UTR region present in *ceh-23p$_L$::mig-6s* was cloned into a *ida1p*::tagRFP plasmid using *KpnI/ApaI* replacing the tag fluorescent protein.	N/A
Plasmid: *ser-2p$_{3s}$::mig-6s*	The *mig-6s* coding and UTR region present in *ceh-23p$_L$::mig-6s* was cloned into a *ser-2p$_3$*::GFP plasmid using *XmaI/ApaI* replacing the tag fluorescent protein.	N/A
Plasmid: *mig-6p*::mNeonGreen::*mig-6s*	A DNA fragment encoding the *mNeonGreen* fluorescent tag was inserted in *mig-6* coding region of *pZH125* using Gibson assembly. The precise insertion site was between S65 and V66 to generate an in-frame insertion located before the first trombospondin domain of MiG-6.	N/A
Plasmid: *mig-6p*::tagRFP	A DNA fragment encoding a *tagRFP* fluorescent tag plus the *unc-54* UTR region was cloned into *pZH125* using *NcoI/ ApaI*. The tag replaced part of exon2, exons 3 to 11 and the *mig-6* 3'UTR and is drove by a 5444bp *mig-6* promoter region.	N/A

REAGENT or RESOURCE	SOURCE	IDENTIFIER
Plasmid: *ida-1p$_{(1.2kb)}$*::GFP	A DNA fragment encoding 1182bp upstream of the ida-1 translational start site was cloned into *pPD95.75* using *Xba*I/*Xma*I.	N/A
Plasmid: *rab-3p::sax-7s*	The *sax-7s cDNA* was cloned from a *dpy-7p::sax-7s* into a *rab-3p*::GFP using *KpnI/ApaI*	N/A
Plasmid: *unc-14p::sax-7s*	Pocock et al. (2008)	N/A
Plasmid: *dpy-7p::sax-7s*	Pocock et al. (2008)	N/A
Plasmid: *ser-2p$_{3s}$::sax-7s*	The *sax-7s* cDNA was cloned from a *dpy-7p::sax-7s* into a *ser-2p$_{-3}$*::GFP using *Kpn*I/*Apa*I	N/A
Plasmid: *ceh23p$_L$::sax-7s*	The *sax-7s* was cloned from a *Pdpy-7::sax-7s* into a *ceh-23p$_L$*::tagRFP using *Kpn*I/ *Apa*I	N/A
Plasmid: *ida-1p$_{(1.2kb)}$::sax-7s*	The *sax-7s* was cloned from a *Pdpy-7::sax-7s* into a *ida-1p::*GFP using *Kpn*I/*Apa*I	N/A
Plasmid: *unc-14p::sax-7s ΔFnIII*	Diaz-Balzac et al. (2015)	N/A
Plasmid: *unc-14p::sax-7s ΔIG*	Diaz-Balzac et al. (2015)	N/A
Plasmid: *unc-14p::sax-7s ΔICD*	The intracellular domain of *sax-7s* was removed by site-directed mutagenesis using the fw primer: cagaattgtcttgaccttgacaacacagcagatgcag and the rv primer: ctgcatctgctgtgttgtcaagggtcaagacaattctg	N/A
Software and Algorithms		
GraphPad (PRISM7)	https://www.graphpad.com/scientific-software/prism/	https://www.graphpad.com/scientific-software/prism/
FIJI	https://fiji.sc/	https://fiji.sc/